JAGIELLONIAN UNIVERSITY IN KRAKOW
Marian Smoluchowski Institute of Physics

A quest for exotic nuclear systems formed in the $^{197}Au + ^{197}Au$ reaction at 23 AMeV

Rafał Najman

A doctoral dissertation
written in the Department of Hot Matter Physics

Thesis advisor:
prof. dr hab. Roman Płaneta

Kraków 2015

Na wstępie chciałem bardzo podziękować wszystkim osobom, którzy przyczynili się do powstania tejże rozprawy. Jako pierwszemu składam serdeczne podziękowania mojemu promotorowi, profesorowi Romanowi Płanecie nie tylko za umożliwienie mi prowadzenia badań, ale przede wszystkim za jego liczne, cenne uwagi, życzliwość i nieustanną motywację w trakcie całego okresu pracy. Dziękuję również dr Ani Sochockiej z Wydziału Fizyki, Astronomii i Informatyki Stosowanej za naszą długoletnią współpracę oraz pomoc w opracowaniu danych.

Chciałbym także podziękować naukowcom z INFN-LNS w Katanii, a w szczególności: Angelo Pagano, Enrico De Filipo, Giuseppe Cardella, Sara Pirrone oraz Paolo Russotto za znaczące wsparcie merytoryczne.

Podziękowania składam również pracownikom Zakładu Fizyki Gorącej Materii: prof. Zbigniewowi Majce, dr hab. Pawłowi Staszelowi, dr hab. Januszowi Brzychczykowi, dr hab. Zbigniewowi Sosinowi, dr hab. Andrzejowi Wielochowi, dr hab. Tomaszowi Kozikowi, Panom inżynierom: Markowi Adamczykowi, Ludomirowi Dutce, Tadeuszowi Barczykowi oraz Pani Elżbiecie Kotuli za wieloletnią współpracę.

Dziękuję także Panu Andrzejowi Grzeszczukowi z Uniwersytetu Śląskiego za udzieloną mi cenną pomoc w początkowym okresie moich badań oraz Tomkowi Capowi z Uniwersytetu Warszawskiego za nasze liczne dyskusje.

Podziękowania należą się tak samo moim kolegom z Instytutu Fizyki: Antoniemu Marcinkowi, Krzysztofowi Pelczarowi, Sebastianowi Kupnemu, Pawłowi Lasko, Jineshowi Kallunkathariyil i Markowi Smaczyńskiemu za wymianę doświadczeń i wszelaką udzieloną mi pomoc.

Chciałbym podziękować prof. Stanisławowi Mickowi z Zakładu Doświadczalnej Fizyki Komputerowej od którego zaczęła się moja przygoda z fizyką.

Praca została częściowo sfinansowana z grantu Narodowego Centrum Nauki (granty: NN202 180638 oraz 2013/09/N/ST2/04383).

Contents

List of Figures

List of Tables

Chapter 1

Introduction

The heaviest natural chemical element existing on Earth is uranium $_{92}U$. All heavier nuclei are produced artificially. Since the beginning of the 30-ies of the 20th century nuclear physicists have been working on synthesis of heavier elements and thinking about how big nuclear objects can be produced. In 1934 Enrico Fermi suggested the method of the superheavy nuclei creation by reactions with neutrons capture. Neutron bombardment of a nucleus (with given Z and N, where Z means proton number and N means neutron number) leads to the creation of the nucleus being an isotope (Z, N+1) of the initial one. This nucleus after β^- decay creates a new element (Z+1, N). The first nucleus created with use of this method was $^{239}_{93}Np$ [1]. In contemporary times, Seaborg and others created plutonium $^{239}_{94}Pu$, bombarding uranium target with deuterons produced in the 150 cm cyclotron [2]. Elements with Z = 99 and 100 were detected for the first time after the hydrogen bomb explosion in 1952. Nuclei with Z = 95, 96, 97, 98, and 101 were created with use of elements of Z = 93, 94, and 99 after neutron or α particle bombardment. In the fifties of the twentieth century beams of nuclei heavier than helium nucleus began to be used for synthesis of heavy elements. Nuclei with $104 < Z \leq 118$ were created in reactions with heavy ions. The lifetimes of the heaviest of them are of the order between several microseconds to several minutes. The question about the maximal mass of atomic nuclei is still open and scientists constantly are trying to find an answer to it. Model calculations suggest the existence of the Island of Stability, where atomic nuclei with some specific proton and neutron numbers should have lifetimes much longer than the others with similar mass and charge located beyond this island [2]. The theoretical predictions, based on above mentioned hypothesis, indicate that the heaviest nuclei should have Z = 118. Is a nucleus with Z = 118 the heaviest one that can exist at least for a very short time?

The latest research may indicate that this is not the case. Alternative method for production of superheavy nuclei was proposed by Majka et al. [3]. The novel experiment is investigating nuclear reaction between heavy projectiles nuclei ($^{172}_{70}Yb$, $^{197}_{79}Au$) and fissible target nuclei ($^{238}_{92}U$, $^{232}_{90}Th$). During nuclear interaction between heavy target and projectile the large mass transfer may occur and, if the conditions for fission are met, some heavy nuclei can be formed. Thus one has the possibility of exploring Super/Hyper Heavy Elements (SHE/HHE) nuclear systems in the regions $112 < Z < 136$. This experiment has been performed in the collaboration between Cyclotron Institute Texas A&M University, Institute of Physics of the Jagiellonian University and the Instituto Nazionale di Fisica Nucleare di Legnaro. The new concept for detection and identification of SHE nuclei (active catcher detection system) has been developed. The method mentioned above is based on implantation and registration of heavy elements in the active catcher detectors, while the high energy α particles originating from decay of heavy elements are detected in the backward detectors. The experiment started in August 2013 and has been continued since then.

Marinov et al. [4] report the Z = 122 nucleus discovery. The mass spectroscopy method applied to thorium ore has shown the occurrence of nuclei with Z = 122 and A = 292. He estimated the abundance of this new element of the order of 10^{-12} when compared to thorium $^{232}_{90}Th$. The lower limit of the half-life of these nuclei was estimated of 10^8 years. Nevertheless, other researchers have not confirmed this results. In a paper Dellinger et al. [5] claimed that the results may have been merely artifacts. Contrary to this conclusion, Marinov et al. [6] allege that there has been no discrepancy between his and Dellinger's results, which confirms the existence of those heavy nuclei.

Hartree-Fock-Bogoliubov model predictions with the Gogny D1S force show that two kinds of exotic hyperheavy nuclei beyond the Island of Stability may exist: true bubbles (stable for masses and charges in the range of 750 - 920 and 240 - 280, respectively) and semi-bubbles that are stable for masses and charges in the range of 292 - 750 and 120 - 240, respectively [7]. The forerunner of this idea was Wheeler who suggested the possibility of some exotic nuclei shapes, such as a bubble or a torus [8, 9].

Siemens and Bethe [10] calculated the binding energy for very heavy nuclear systems (masses up to 3000) with various exotic shapes like: spherical shell, oblate and prolate spheroid. They showed that these systems with suitably large electric charge (greater than 104) are the most β-stable when they are prolate spheroids.

Wong pointed out on the dependence of system existence probability on temperature [11]. The temperature increase lessens the value of surface tension coefficient and Coulomb interaction pushes the nuclear matter outwards. The effect leads to formation of toroidal or bubble nuclei. Moretto showed that charge-emptied central cavity in a bubble-shaped nucleus makes it stable against monopole oscillations [12]. Such objects are not stable against quadrupole or octupole oscillations. Calculations performed within the framework of rotating charged drop model show that for nuclei with masses of 300 - 350, potential energy minimum occurs for toroidal-shapes even if nuclear angular momentum is zero [13]. Also the shell model predicts the existence of α, β and fission-stable bubble-shaped nuclei with masses A = 450 - 2000 and charges Z = 325 - 400 [14].

The different approach to this issue was proposed by Warda [15]. The stability of heavy nuclear systems as a function of quadrupole moment $\hat{Q}_2$ was investigated. It was shown that the energy of the toroidal minimum decreases relatively to the potential energy of the spherical configuration with increase of the mass of the system. It was found as well that for nuclei with $Z > 140$ the global energy minimum corresponds to toroidal-shapes. In contrast to bubble nuclei, the synthesis of toroidal nuclei is experimentally available in collisions between stable isotopes.

In order to create toroidal nuclei, it is necessary to form toroidal freeze-out configurations in heavy ion collisions which may lead to such creation. The formation of such configurations is the subject of my dissertation.

Simulations using models BUU (Boltzmann-Uehling-Uhlenbeck) and BNV (Boltzmann-Nordheim-Vlasov) for heavy ion collisions show that toroidal and bubble nuclei can be formed in central and semi-central collisions. Such simulations have been performed for various colliding systems at a wide energy range [16].

Hydrodynamic calculations show that formation of toroidal objects is quite common in nature [17]. Kuo-Long Pan et al. [18] studied binary droplet collisions of liquids with various viscosities and surface tension at wide-range of Weber number (We) which is proportional to the droplet diameter and initial impact energy. The experiment was performed for We values from 58 to 5100 which corresponds to the relative droplets velocity V_r from 2.45 to 23 $\frac{m}{s}$ and the droplets diameter D equal to 0.7 mm. At the collision sequences of two water droplets for splattering at the expanding phase with We = 805.2 ($V_r = 9.10\frac{m}{s}$, D = 0.70 mm) the toroidal-shape objects were observed.

In nuclear collisions, there have been suggested various observables that are characteristic for exotic shape nuclear system decay:

- the observed number of fragments with intermediate masses should be greater than the number of fragments coming from spherical nuclei at the constant temperature of decaying system [19];
- the observed fragments should be of similar sizes; the models predict that exotic shape systems most probably decay emitting fragments with similar masses [20, 21];
- the sphericity parameter for collisions with emitted fragments should have low values [19].

So far collected evidences that prove exotic shape nuclear system decay are very limited. Stone et al. [22] presented the experimental data set for the reaction $^{86}Kr +^{93} Nb$ at energies between 35 to 95 MeV/nucleon. In order to distinguish between toroidal and bubble-shape freeze-out configurations decay they investigated behavior of several used signatures as a function of incident energy. They observed anomalous increase of the number of intermediate-mass fragments, an enhanced similarity of the charges of large fragments and suppressed sphericity of the emission of heavy fragments in the beam energies region between 60 and 75 MeV/nucleon. The authors have interpreted obtained results as experimental evidences for the toroidal system breakup. Jouault and others [23] worked on the reactions $Pb + Au$ and $Pb+Ag$ at energy of 29 MeV/nucleon. They investigated the correlation between velocity, kinetic energies of the fragments and the charge of these fragments. In case of $Pb + Au$ reaction the velocity distribution is narrow and the kinetic energy increases regularly with charge, while for $Pb + Ag$ velocity distribution is broad and there is the maximum on the kinetic energy distribution for intermediate charges. For the $Pb + Au$ reaction authors interpreted obtained results as a breakup of the hollow source intermediate between toroidal and bubble-like, while for $Pb + Ag$ reaction they assume the formation of roughly ellipsoidal system.

To determine the optimal conditions for formation of toroidal-shape nuclear systems for $Au + Au$ collisions, simulations were performed in a wide range of incident energies using the BUU code [24]. These calculations indicate that the threshold energy for the formation of toroidal nuclear shapes is located around 23 MeV/nucleon.

Modern detector systems with large acceptance give great opportunities to perform very precise measurements of heavy ion collision products. It is possible to obtain more detailed characteristic of investigated reaction. The present work is focused on search of the exotic shape nuclear systems formed in the $^{197}Au +^{197} Au$ reaction at 23 AMeV and the identification of emitted fragments with use of CHIMERA 4π multidetector [25] available at INFN-LNS in Catania, Italy.

The thesis is organized as follows: in Chapter 2 the CHIMERA multidetector is briefly described including its design and electronics chains. In Chapter 3 the calibration procedures and utilized identification techniques are described. In Chapter 4 some global experimental observables and correlations are shown. The region of well defined events, where almost all particles from investigated reaction were correctly identified, was also defined. The Chapter 5 includes theoretical predictions pointing at the existence of exotic configurations in the framework of static and dynamic models. This Chapter also contains the definitions of shape sensitive observables which were used to determine the shape of the created nuclear system. The methods used in order to reduce non-central collisions have been described. The comparison between experimental data and theoretical models is also shown. In Chapter 6 we summarize the results of research performed.

Chapter 2

Experiment details

The experiment was performed at INFN-LNS (**I**nstituto **N**azionale di **F**isica **N**ucleare - **L**aboratori **N**azionali del **S**ud) in Catania in Sicilia, Italy, using the CHIMERA (**C**harged **H**eavy **I**on **M**ass and **E**nergy **R**esolving **A**rray) multidetector. The total number of collected events is of the order of 10^8. In our experiment the beams were delivered by two accelerators (see Fig. 2.1):

- 15MV Tandem Van De Graaff;
- K800 Superconducting Cyclotron.

The LNS Tandem accelerator (after many improvements) is characterized by maximum operational voltage of 15 MV, good reliability and excellent transmission which reaches about 100%. The maximum energy goes from 105 MeV for carbon and 135 MeV for oxygen to 200 MeV for heavier ions.

The LNS Superconducting Cyclotron is characterized by the radius equal 90 cm. Its magnetic field varies in the range of 2.2 to 2.8 T. The magnet coils are made of an Nb-Ti alloy and are operated at liquid helium temperature. The nuclei are accelerated to energies of 100 and 20 MeV/nucleon for the light and heaviest ions respectively.

2.1 The CHIMERA detector

The LNS laboratory possesses a powerful detector system - multidetector CHIMERA. The multidetector CHIMERA [25] is an array of 1192 detection cells, arranged in cylindrical geometry around the beam axis and grouped together in 35

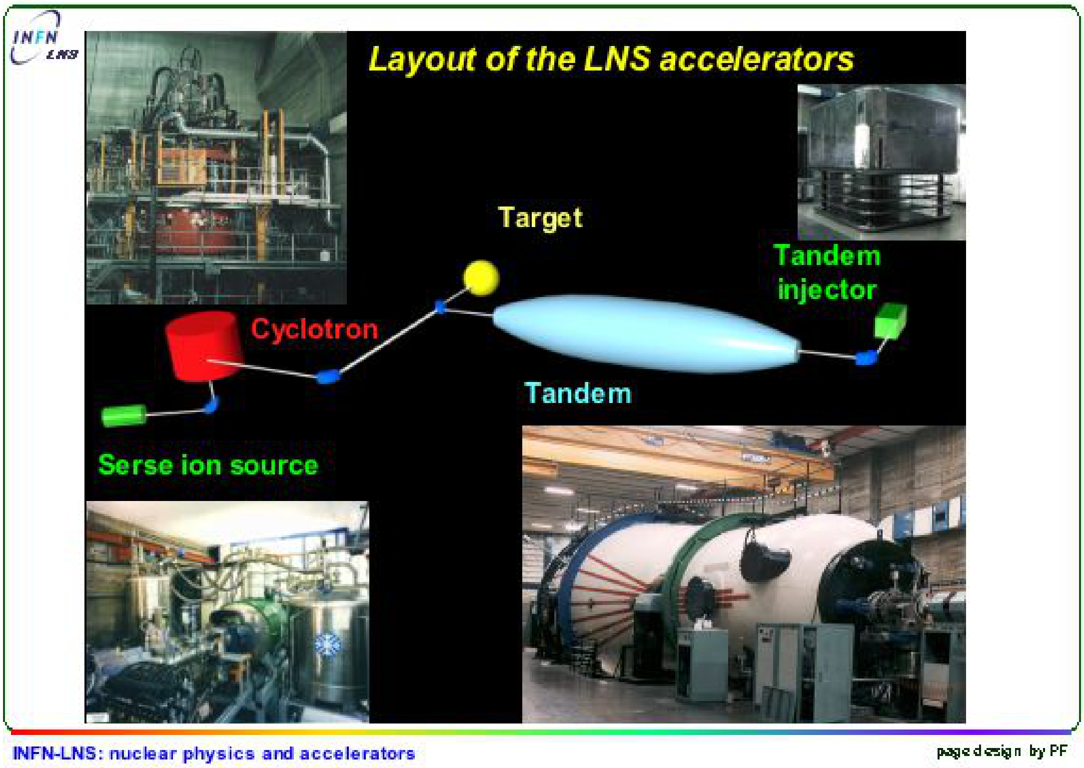

Figure 2.1: Layout of the INFN-LNS accelerators.

rings (see Fig. 2.2). The first 687 telescopes belonging to the 18 front rings are assembled on 9 wheels and cover the polar angles up to 30°.

Each ring, depending on the polar angle θ_{lab} value, is divided into 16, 24, 32, 40 or 48 trapezoidal modules arranged at various azimuthal angles ϕ. The distances from these detectors to target change with θ angle from 350 cm (the first ring detectors) to 100 cm (the 9-th ring detectors). The remaining 17 rings cover the angular range from 30° to 176° and create a sphere with a 40 cm radius. The overall detection solid angle is about 94% of 4π. The large granularity ensures a low probability of multi hits and the large solid angle in connection with the low energy detection threshold give the good capabilities to an event reconstruction. Geometrical characteristics of CHIMERA detector modules are presented in Table 2.1.

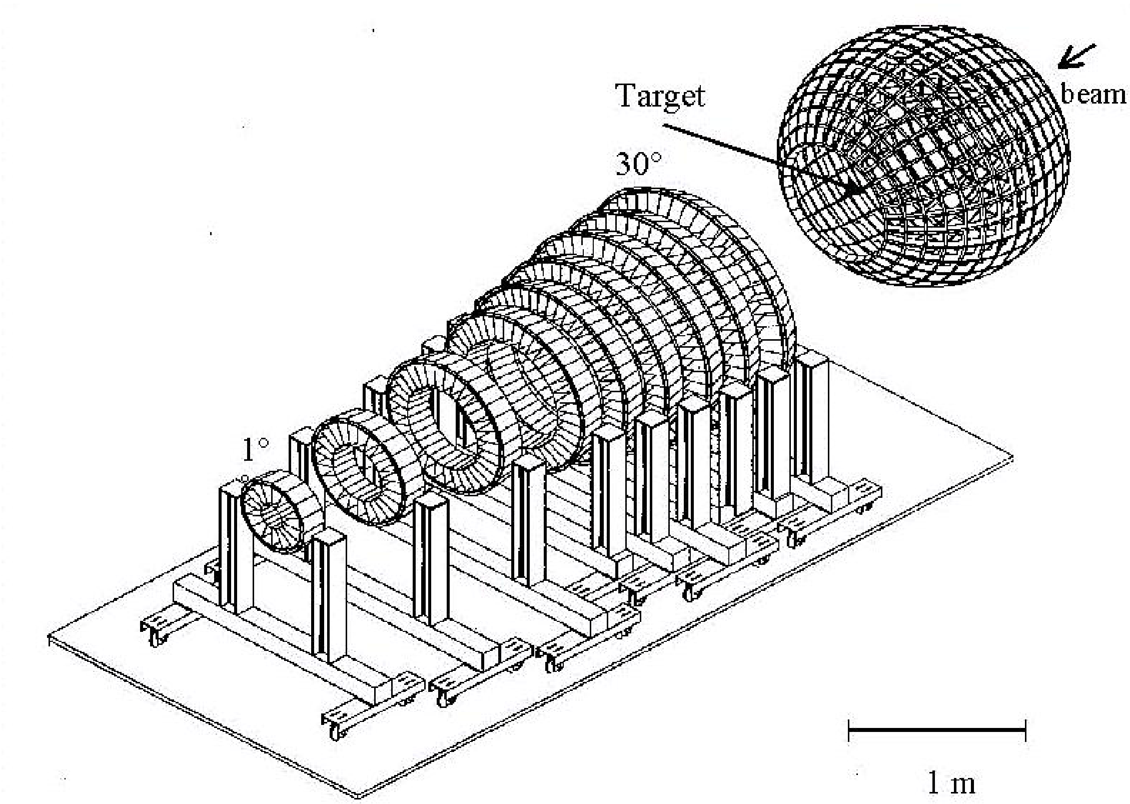

Figure 2.2: Schematic view of the CHIMERA multidetector.

Each detection cell is composed of two detectors (see Fig. 2.3). The first element is a silicon (Si) detector of a thickness from 195 to 320 μm (average is 280 μm). The Si detectors applied in CHIMERA stand out their well-defined, homogeneous

Rings	Modules	Distance (cm)	θ_{mean} (°)	$\Delta\theta$ (°)	$\Delta\phi$ (°)	Surface (cm^2)	$\Delta\Omega$ (mSr)
1-I	16	350	1.40	0.8	22.50	16.3	0.133
1-E	16	350	2.20	0.8	22.50	25.6	0.209
2-I	24	300	3.10	1.0	15.00	22.2	0.247
2-E	24	300	4.10	1.0	15.00	29.3	0.326
3-I	32	250	5.20	1.2	11.25	23.3	0.373
3-E	32	250	6.40	1.2	11.25	28.6	0.458
4-I	40	210	7.75	1.5	9.00	24.2	0.549
4-E	40	210	9.25	1.5	9.00	29.1	0.660
5-I	40	180	10.75	1.5	9.00	24.8	0.765
5-E	40	180	12.25	1.5	9.00	28.2	0.870
6-I	48	160	13.75	1.5	7.50	20.8	0.813
6-E	48	160	15.25	1.5	7.50	23.1	0.902
7-I	48	140	17.00	2.0	7.50	26.2	1.337
7-E	48	140	19.00	2.0	7.50	29.1	1.485
8-I	48	120	21.00	2.0	7.50	23.6	1.639
8-E	48	120	23.00	2.0	7.50	25.7	1.785
9-I	48	100	25.50	3.0	7.50	29.5	2.950
9-E	48	100	28.50	3.0	7.50	32.7	3.270
S10	32	40	34.00	8.0	11.25	24.5	15.313
S11	32	40	42.00	8.0	11.25	29.3	18.313
S12	32	40	50.00	8.0	11.25	33.6	21.000
S13	32	40	58.00	8.0	11.25	37.2	23.250
S14	32	40	66.00	8.0	11.25	40.1	25.063
S15	32	40	74.00	8.0	11.25	42.2	26.375
S16	32	40	82.00	8.0	11.25	43.4	27.125
S17	32	40	90.00	8.0	11.25	43.9	27.438
S18	32	40	98.00	8.0	11.25	43.4	27.125
S19	32	40	106.00	8.0	11.25	42.2	26.375
S20	32	40	114.00	8.0	11.25	40.1	25.063
S21	32	40	122.00	8.0	11.25	37.2	23.250
S22	32	40	130.00	8.0	11.25	33.6	21.00
S23	32	40	138.00	8.0	11.25	29.6	18.313
S24	32	40	146.00	8.0	11.25	24.5	15.313
S25	16	40	156.50	13.0	22.50	56.7	35.438
S26	8	40	169.50	13.0	45.00	50.9	31.813

Table 2.1: CHIMERA geometrical features and detectors definitions: ring number, number of modules, distance from a target, mean polar angle, polar range, azimuthal range, surface, solid angle respectively.

thickness and a well-defined active zone. The passivated surfaces are protected by $3\mu m$ polymer layer. The detector thicknesses have been chosen to ensure the optimization of identification methods. The resistance and capacity are 3000-5000 $\Omega \cdot cm$ and 500-2200 pF, respectively.

The second detector is a thick thallium doped cesium iodide crystal CsI(Tl) located on the back and equipped with a photodiode recording the light generated during the passage of a particle through the detector. When the polar angle increases, the thickness of the crystals decreases from 12 to 3 cm. They are used to measure the remaining energy for particles passing through the Si detector. The CsI(Tl) crystal is an ideal detector registering light charged particles. Its density($4.51\frac{g}{cm^3}$) allows the full stopping of the light charged particles comparing to other, less dense detectors. In the CHIMERA multidetector the scintillators are coupled to photodiodes for the light readout. The photodiodes ensure good stability, easy installation and low power consumption.

A single particle gives two signals from cesium iodide (fast and slow) and three from silicon detector (time and two energy signals). All the system operates in vacuum ($8.7 \cdot 10^{-7} mbar$) and it is thus installed in the dedicated chamber (see Fig. 2.4).

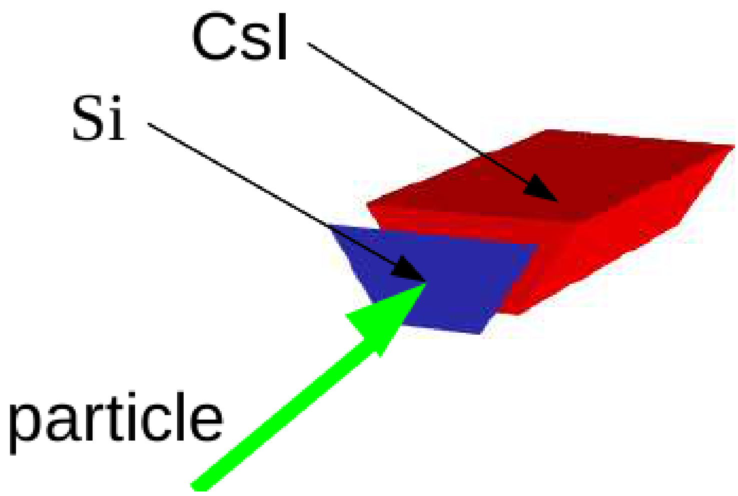

Figure 2.3: Schematic view of the detection module.

To identify the registered fragments three methods are in use:

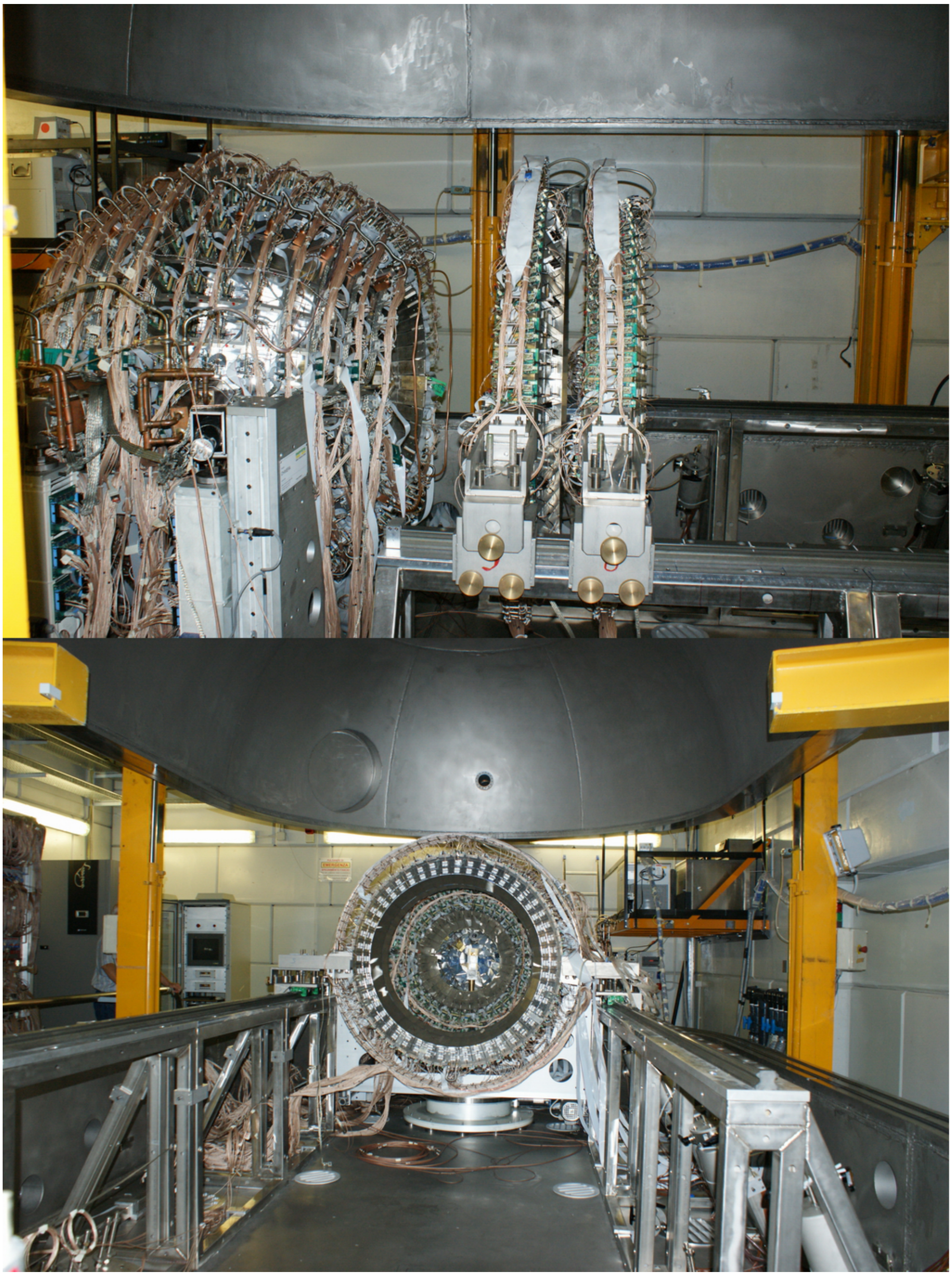

Figure 2.4: Photos of the CHIMERA multidetector with partially disassembled front rings.

- the Time of Flight (ToF) method allows to determine the mass of fragments stopped in the Si detector using the time signal coming from the Si-detector and the reference cyclotron signal;
- the $\Delta E - E$ method allows to determine the particles charge using the signals from Si and CsI(Tl) detectors;
- the Pulse Shape Discrimination (PSD) method in CsI(Tl) detectors allows to identify light charged particles (p, d, t, ^3He, α, Li) using the fast and slow components of scintillator signal.
- the PSD method in Si detectors allows to identify particles stopped in the silicon detectors. This method gives good charge identification from α particle up to the F nucleus.

In Table 2.2 the identification techniques are classified. In our analysis we identified fragments using ToF and $\Delta E - E$ methods. Due to limited manpower the identification of light particles using PSD method will be done in future.

Energy (MeV/nucleon)	Technique	Measure
Fragments ($Z > 3$)		
5 - 12	PSD Si	Z
$<$ 12-15	ToF	A
$>$ 12-15	$\Delta E - E$	Z
Light particles ($Z \leq 3$)		
$<$ 6	ToF	A
$>$ 6-30	$\Delta E - E$	A, Z
$>$ 20	PSD CsI(Tl)	A, Z

Table 2.2: Identification methods for fragments and light particles for different energy ranges in the CHIMERA detector.

2.2 Electronics

The signals coming from Si and CsI(Tl) detectors are processed by electronics chains and transformed to the form acceptable by the acquisition system. Electronic circuits are similar for both detector types. They are shown in Fig. 2.5 (from

Ref. [26]). Pre-amplifiers of Si detectors and photodiodes are placed on electronic plates inside the vacuum chamber to minimize the signal loss and reduce electronic noise. The system is cooled by a circulating liquid ensuring, despite the heat release, the stable system operation. The voltage generators for detectors and pre-amplifiers are placed outside the vacuum chamber.

The signals from Si detector are first pre-amplified by a Pulse Amplitude Converter (PAC). The detector signal is integrated, the output signal is independent of the detector capacity and proportional to the charge of the particle. The input signal carries information on the energy and time. The input and output signals have opposite signs. The rise and decay times of the output pulse are $50ns$ and $200\mu s$ respectively. The pre-amplifier is equipped with an input test. The amplifiers sensitivity changes with the polar angle. In the front section, where the high energy particles are expected, it is of the order of $2\frac{mV}{MeV}$, while on the sphere $4.5\frac{mV}{MeV}$. In both cases, the output signal is lower than 8V. Each channel produces time and energy signals. The time signal is sent to a discriminator and the energy signal is coded by QDC (Charge Digital Converters). In order to provide a good energy resolution both for high and low energy signals, the signals are double coded: High Gain (HG) and Low Gain (LG). High Gain coding is applied when the integrated charge of passing particle is less then $\frac{1}{8}$ of full charge dynamical range. The CFD (Constant Fraction Discriminator), placed in CAMAC modules, is used to measure time. The swift discriminator output signal is the TDC (Time to Digital Converter) input signal.

In the CsI(Tl) detectors electronic chain the connection photodiode-crystal makes it possible to receive an effective detector reading, similar to readings from Si detectors. The charge pre-amplifiers for photodiode signal are used together with a coupled capacitor, which improves the light collecting. The pre-amplifier signals are then amplified and shaped with various rise times (0.5, 1, 2, and $3\mu s$). Two output energy signals are directed to QDC (amplification = 10) and stretchers (amplification = 1) to integrate the slow and fast component of the CsI(Tl) signal respectively. The time output has amplification 15. More details about CHIMERA one can find in [26].

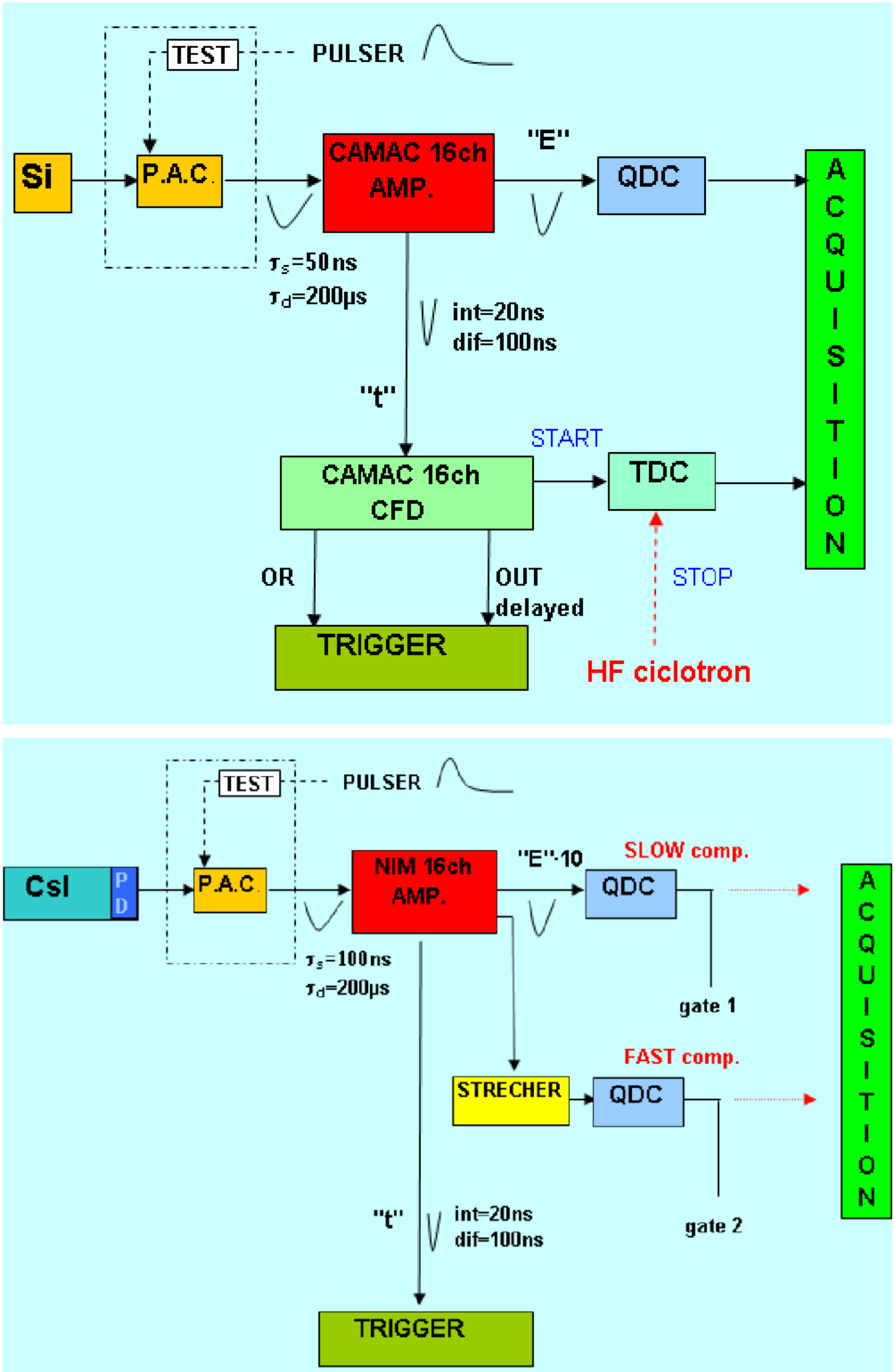

Figure 2.5: The front-end electronic of silicon (top panel) and CsI(Tl) (bottom panel) detectors.

Chapter 3

Calibration procedures

The collected data are calibrated using a set of dedicated programs partially developed at LNS-INFN. Our calibration procedure include:

- energy calibration of Si detectors;
- charge identification of fragments;
- mass identification of fragments.

3.1 Pulser calibration

As it was mentioned in Subchapter 2.2, the energy signals from Si detectors are double coded (High Gain and Low Gain). In order to obtain the voltage to channel relation of the ADC (Analog-to-Digital Converter) for each detector, the ADC calibration using pulser runs was performed. The calibration was done both in HG and LG range (see Fig. 3.1). There is a two-parameter linear dependence between HG and LG signals. The transformation of the signal x (in QDC channel) to voltage in mV is as follows:

$$\begin{aligned} V_{HG}(x) &= a_{HG} \cdot x + b_{HG}, \\ V_{LG}(x) &= a_{LG} \cdot x + b_{LG}. \end{aligned} \tag{3.1}$$

Typical linear fits of the HG and LG signals for detector 81 are shown in Fig. 3.2. The conversion from HG to LG can be performed based on following relation:

$$Ch_{LG} = \frac{Ch_{HG}}{Gain} + offset, \tag{3.2}$$

where Ch_{LG} is signal codified in LG, Ch_{HG} is signal codified in LG, the quotient $\frac{a_{LG}}{a_{HG}}$ is called Gain and it represents the ratio of ADC ranges (HG and LG), while $offset = \frac{b_{HG}-b_{LG}}{a_{LG}}$ is a distance between HG and LG lines at V=0.

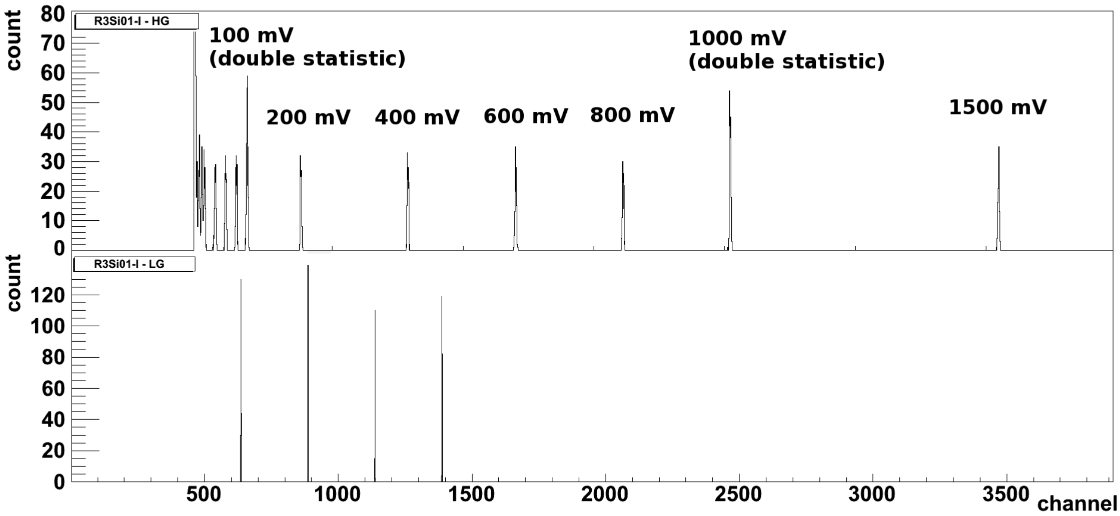

Figure 3.1: Pulser spectra for HG (top panel) and LG (bottom panel) for detector 81 located at $\theta = 5.2°$.

3.2 Energy calibration

In order to perform the conversion from ADC channel to MeV the energy calibration of Si detectors was done. Energy calibration was performed using ion beams fully stopped in Si detectors, delivered both by the tandem and the cyclotron. The data for the following systems were used:

- the elastic scattering data for $^{16}O + Au$ at 60 and 80 MeV, $^{58}Ni + Au$ at 142 MeV, $Au + Au$ at 170 MeV and 23 AMeV;
- recoil peak for $Au +^{12} C$ at 170 MeV;
- fission fragments from $Au +^{12} C$ reaction at 23 AMeV;
- pedestal (channel number with energy value equal zero).

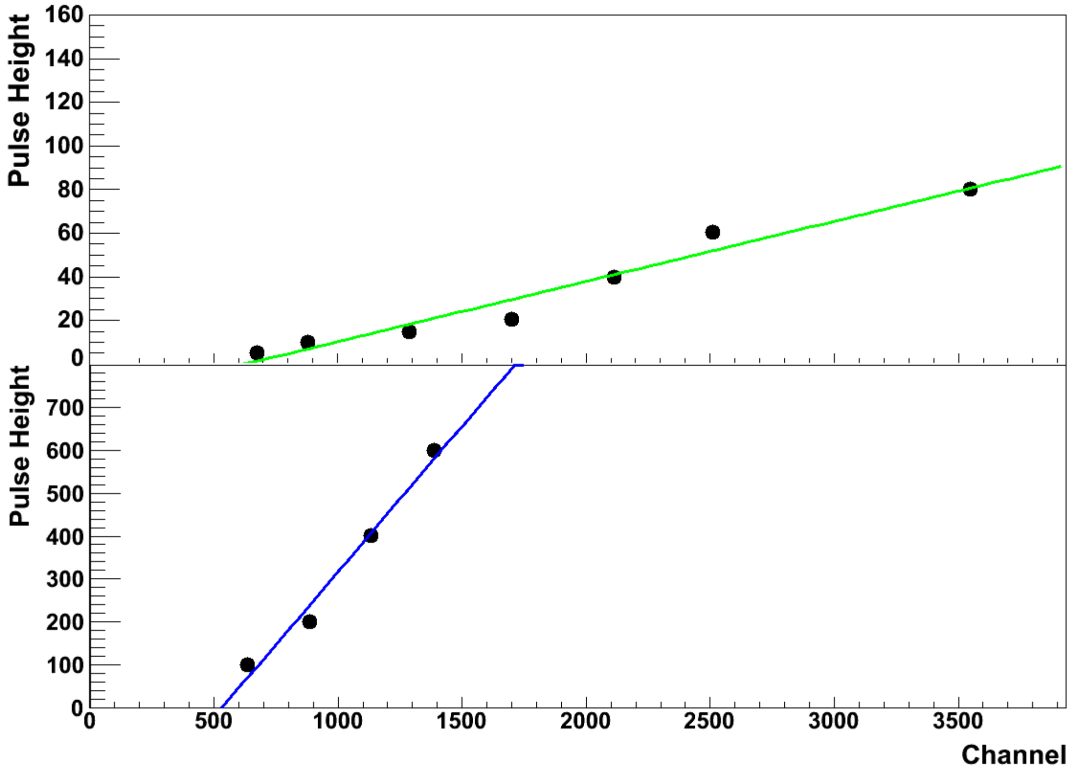

Figure 3.2: Linear fits for HG (top panel) and LG (bottom panel) for gain and offset for detector 81 located at $\theta = 5.2°$.

The channel to energy relation is defined as follows:

$$E(x) = A \cdot x + B, \tag{3.3}$$

where x is channel number, A and B are linear coefficients. Before fitting procedure, all data points were transformed to HG range. The result of energy calibration for detector 211 located at $\theta = 9.25°$ is shown in Fig. 3.3.

3.2.1 Pulse Height Defect

In the silicon detectors one can observe the differences between the pulse height produced by a heavy ion depositing the same energy as the lighter one [27]. This non-linear effect is referred to as Pulse Height Defect (PHD) and was taken into account during Si detectors energy calibration. There are several processes which cause PHD:

- loss of energy in the dead layer of the detector;
- recombination process (when high-density of carriers is generated by strongly ionizing particles);
- the ballistic deficit (the electric field strength is diminished by the space charge of the local plasma, the collection velocity is reduced and the rise time of the output signal is increased).

In our calibration procedure PHD was parametrized by a power law [28]:

$$PHD = 10^{b(Z)} E^{a(Z)}, \tag{3.4}$$

where the power indexes a(Z) and b(Z) are given by:

$$\begin{aligned} a(Z) &= 0.0223(Z^2/10^3) + 0.5682, \\ b(Z) &= p1 + p2(10^2/Z), \end{aligned} \tag{3.5}$$

where p1 = 0.0825 and p2 = -0.1425 coefficients were used. Finally the true energy, E_{true}, is as follows:

$$E_{true} = E_{obs} + PHD. \tag{3.6}$$

where E_{obs} is the expected observed energy.

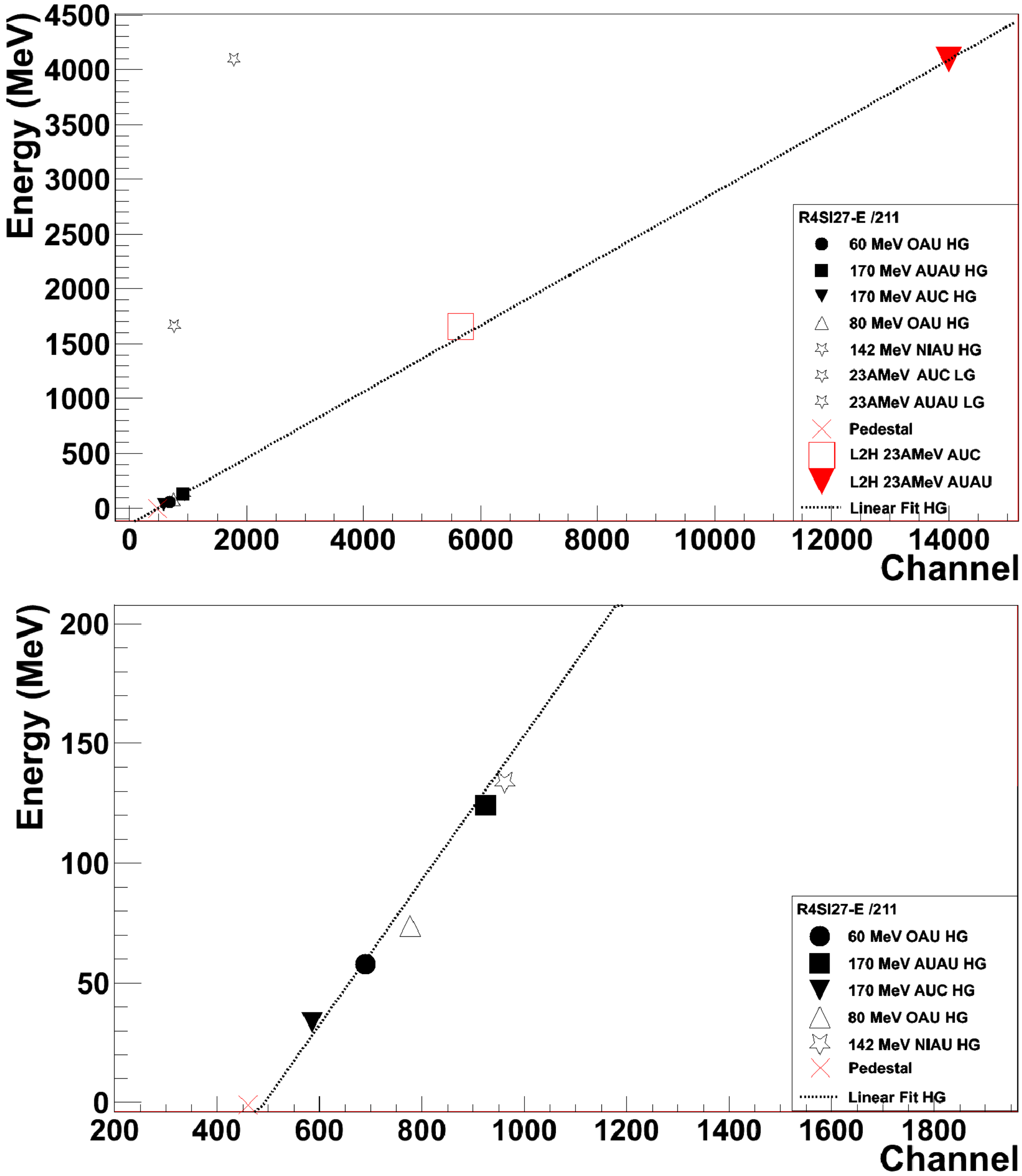

Figure 3.3: The energy calibration line for detector 211 located at $\theta = 9.25°$.

If the particle has high atomic number there is a visible difference between the true energies deposits in silicon and the observed energies (see elastic scattering for $Au + Au$ reaction on Fig. 3.4).

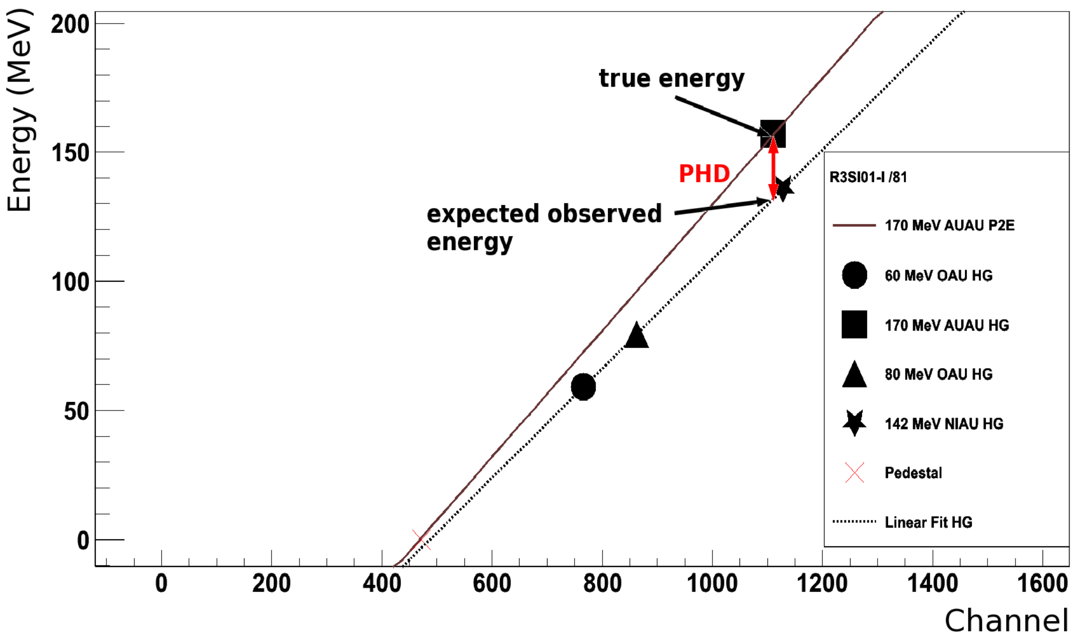

Figure 3.4: The energy calibration line with well-described PHD for detectors 81 located at $\theta = 5.2°$.

3.3 Charge identification technique

In order to identify fragments punching through the silicon detector, we employ the $\Delta E - E$ technique. This method allows to identify atomic number Z and it is based on the correlation between signals coming from the Si (ΔE_{Si} signal) detector and from CsI(Tl) crystal (residual energy $E_{R,CsI}$) for each charge value (see Fig. 3.5):

$$E = \Delta E_{Si} + E_{R,CsI}. \tag{3.7}$$

In Fig. 3.6 an example of $\Delta E - E$ plot is shown for a detector belonging to the 3-th internal ring, at a polar angle $\theta = 5.2°$. The observed correlation can be parametrized using the 14 parameters functional and it is based on the Bethe-Block

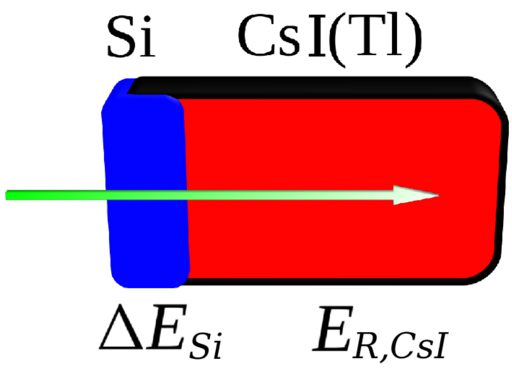

Figure 3.5: $\Delta E - E$ technique.

formula [29]. The Z spectra of fragments observed by the telescope located on the ring at $\theta = 5.2°$ and on the sphere at $\theta = 42°$ are presented in Fig. 3.7 (top and bottom panel, respectively). We can see that in the Z spectrum corresponding to the telescope located at small angle good charge identification can be observed up to Z=40. For higher charges due to limited statistic it is difficult to select lines corresponding to individual Z value for a given detector. Going to large observation angles the charge distributions are much steeper.

3.4 Mass identification technique

For the class of particles stopped in Si detectors the Time of Flight (ToF) identification method is used. The start signal is given by 30% Constant Fraction Discriminator acting on time signal generated by the silicon detector, while the stop signal is given by delayed Reference Signal delivered by the cyclotron. The ToF technique is based on the time difference between those two signals. In this case mass values are calculated using the formula:

$$m = \frac{2E(t_0 - t)^2}{R^2}, \tag{3.8}$$

where R is the distance between the target and a given detector, t is the measured time it takes the particle to travel from the target to the detector and the t_0 is a time offset (caused by cables and cyclotron phase, pulse delay in Si detectors and other effects) of the measured time t.

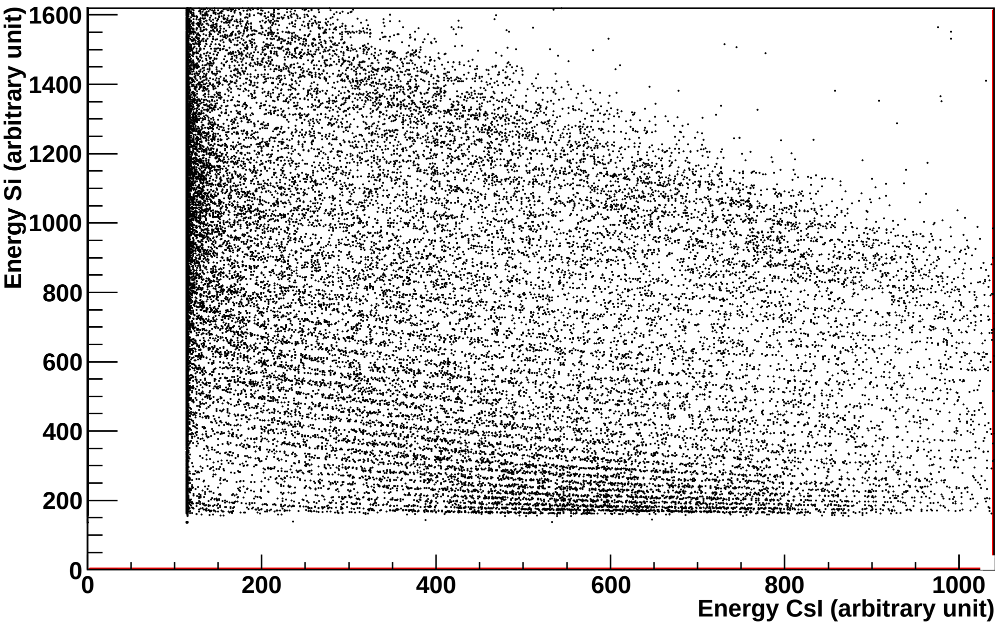

Figure 3.6: $\Delta E - E$ for fragments detected in telescope located at $\theta = 5.2°$.

The values of the time offset t_0 are dependent on incident energy and mass of the observed particle detected in silicon detectors [30, 31]. The t_0 values for well identified light fragments and Au-like nuclei fragments located at the left-hand-side edge of the $\Delta E - time$ distribution (see Fig. 3.8) are presented by color symbols in Fig. 3.9. In our analysis this dependence for each detector was parametrized by the phenomenological formula:

$$t_0 = \begin{cases} t_{0,sat} & t_{0,sat} < \Delta t \\ t_{0,sat} - \Delta t & t_{0,sat} > \Delta t, \end{cases} \tag{3.9}$$

$$\Delta t = B - A(1 - exp(\gamma m)) \cdot (\frac{E}{E_{PT}})^{(\alpha - \delta m)} \cdot exp(-(\frac{E + (\beta + \mu m)E_{PT}}{E_{PT}})^{\epsilon}),$$

where $t_{0,sat}$ is determined for particles punching through the silicon detector. The E_{PT} is the highest energy deposited by particles with mass m. These values were calculated using Physical Calculator from LISE++ program developed by LISE++ group at NSCL/MSU [32]. The E_{PT} values for experiment and theoretical calculations for Si detector with thickness equal 290 μm are presented in Table 3.1.

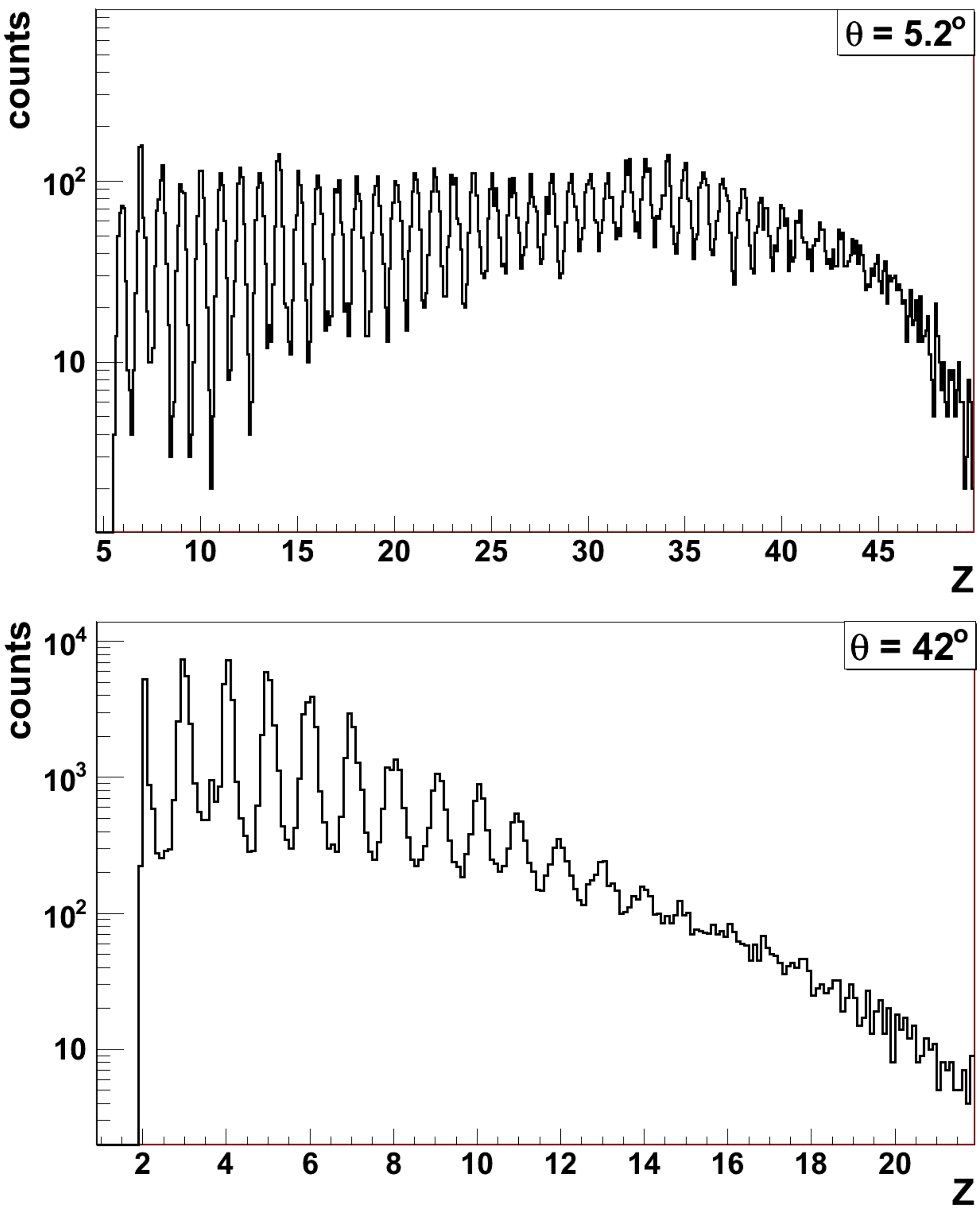

Figure 3.7: Z spectra for fragments observed in telescope on 3-th internal ring located at $\theta = 5.2°$ (top panel) and in telescope on 2-nd ring on the sphere located at $\theta = 42°$ (bottom panel).

The values of the parameters A, B, $\alpha, \beta, \gamma, \delta, \mu$ and ϵ were established in the fitting procedure. The fitting procedure results are represented by solid lines in Fig. 3.9.

E_{PT}^{exp}	A,Z	E_{PT}^{LISE++}
23 ± 1	4, 2	23
47 ± 2	7, 3	48
75 ± 3	9, 4	74
103 ± 3	11, 5	103
136 ± 3	13, 6	135
172 ± 7	15, 7	171
213 ± 5	17, 8	208
258 ± 4	19, 9	248
298 ± 6	21, 10	290
341 ± 8	24, 11	339
385 ± 8	26, 12	385

Table 3.1: The experimental E_{PT} values together with theoretical calculations for Si thickness equal 290 μm

Inserting equation (3.9) into (3.8) the masses of particles were calculated in the iterative procedure (see Fig. 3.10). In frame of this procedure fragment energies were corrected for pulse height defect and charge values were estimated using the EPAX formula. Results of this procedure are shown in Fig. 3.11, where calculated positions for selected mass numbers are presented together with experimental $\Delta E - time$ distributions for telescopes located at angles $\theta = 17^{\circ}$ and 28.5°. In Fig. 3.12 two-dimensional mass versus kinetic energy distributions are shown for telescopes located at two angular regions. At $3^{\circ} < \theta < 10^{\circ}$ the distribution extends from small masses seen at low energies up to the Au elastic peak. At a larger angle the particles with masses up to 200 a.m.u. are observed at relatively low kinetic energies.

3.5 Semi-empirical mass formulas

In order to calculate mass for given Z value extracted from $\Delta E - E$ method and Z value for given mass extracted from ToF method, we have applied the Charity [33] and EPAX [34] formulas. The Charity parametrization is based on light particle

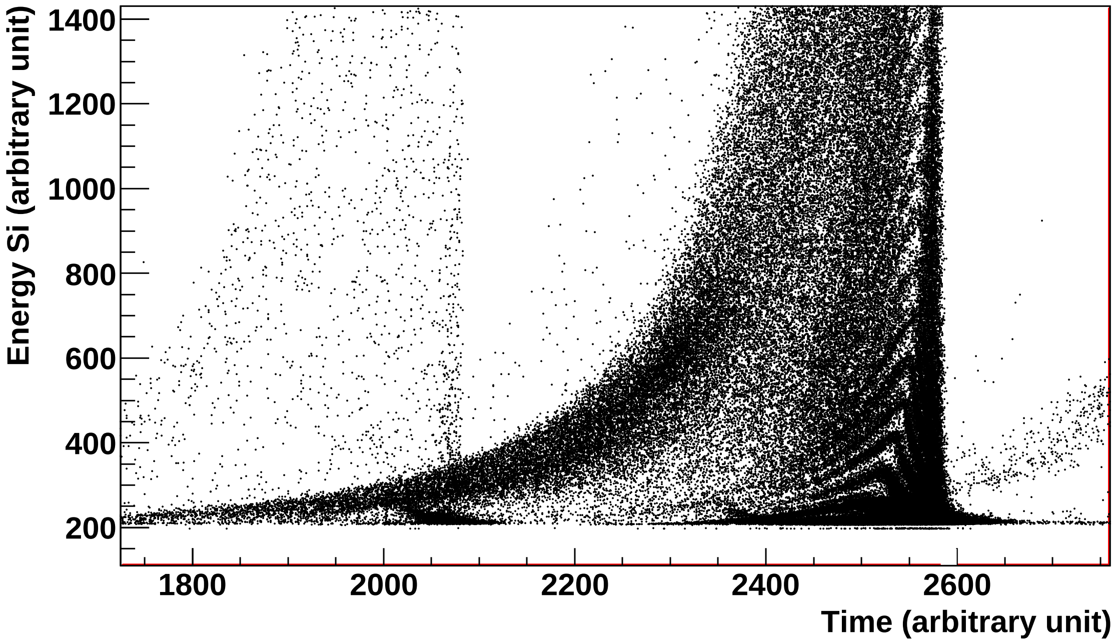

Figure 3.8: $\Delta E - time$ spectrum for fragments detected in telescope located at $\theta = 28.5°$.

evaporation process, while the EPAX is an empirical parametrization based on fragmentation cross section.

The Charity formula is defined as:

$$A(Z) = \begin{cases} 2.072Z + 2.32 \cdot 10^{-3} Z^2 & Z > 4 \\ 9 & Z = 4 \\ 7 & Z = 3 \\ 4 & Z = 2 \\ 1 & Z = 1 \end{cases} \tag{3.10}$$

The EPAX formula is defined as:

$$Z(A) = Z_\beta(A) + \Delta + \Delta_m, \tag{3.11}$$

$$Z_\beta(A) = \frac{A}{1.98 + 1.55 \cdot 10^{-2} A^{2/3}}, \tag{3.12}$$

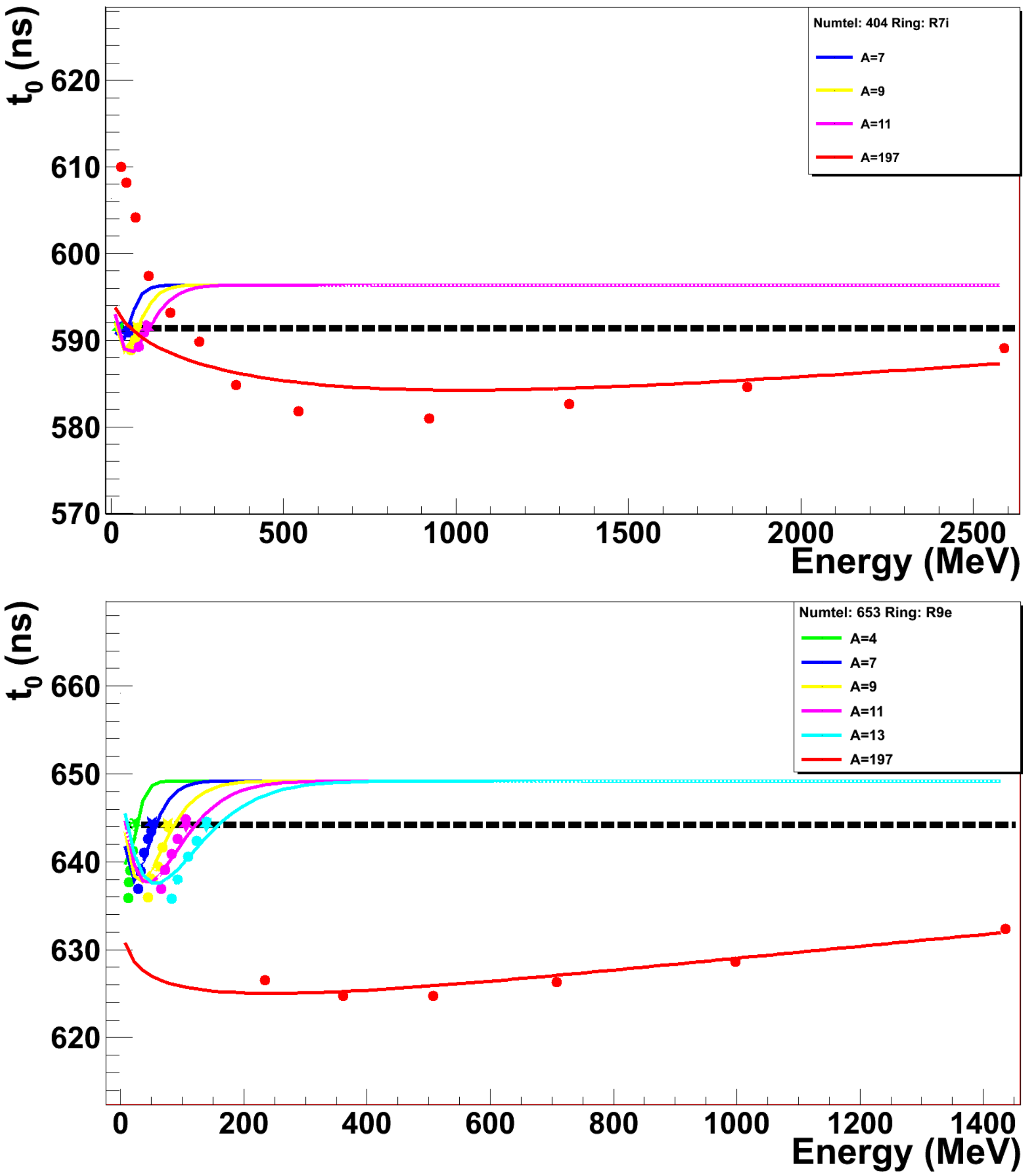

Figure 3.9: The t_0 parameter dependence on incident energy and particle mass for telescopes 404 (top panel) and 653 (bottom panel) located at $\theta = 17°$ and $28.5°$, respectively. Color symbols represent the t_0 values for identified light fragments and Au-like fragments. Solid lines represent the fitting results using formula 3.9. The dashed line indicate the $t_{0,sat}$ value. Star symbols correspond to the punch through energies for identified fragments.

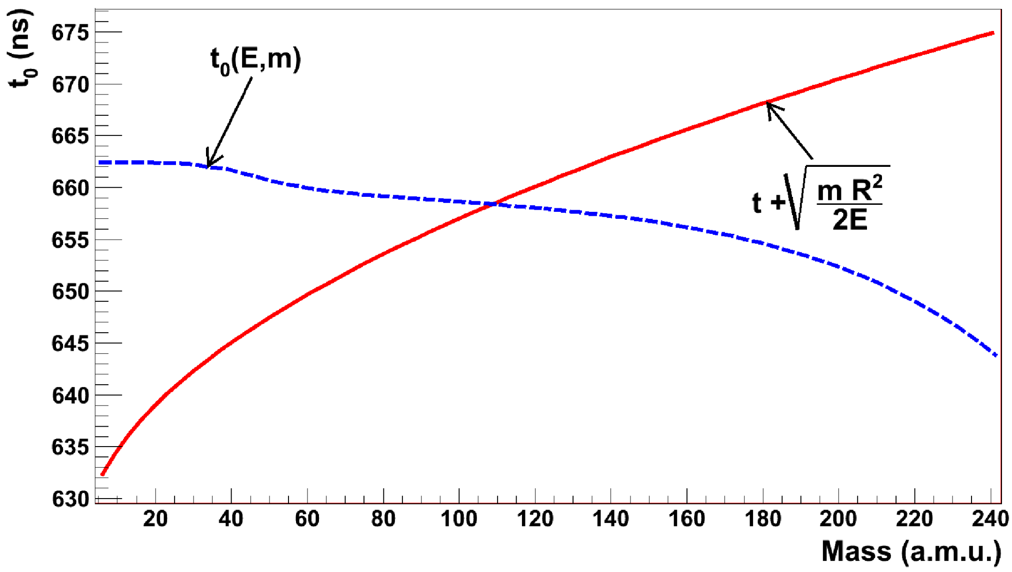

Figure 3.10: Graphical presentation of the equation: $t_0(E, m) = t + \sqrt{\frac{mR^2}{2E}}$ used for mass determination.

$$\Delta = \begin{cases} 2.041 \cdot 10^{-4} A^2 & A < 66, \\ 2.703 \cdot 10^{-2} A - 0.895 & A \geq 66, \end{cases} \tag{3.13}$$

$$\Delta_m(A) = (0.4(A/A_t)^2 + 0.6(A/A_t)^4)\Delta_\beta(A_t), \tag{3.14}$$

$$\Delta_\beta(A_t) = Z_t - Z_\beta(A_t). \tag{3.15}$$

In the Fig. 3.13 one can see the comparison of above mentioned parameterizations. For gold nucleus (Z=79), the EPAX formula delivers mass 185, while the Charity formula delivers mass 179. One can see that the EPAX formula gives mass closer to projectile (197). In our analysis we decided to use this formula.

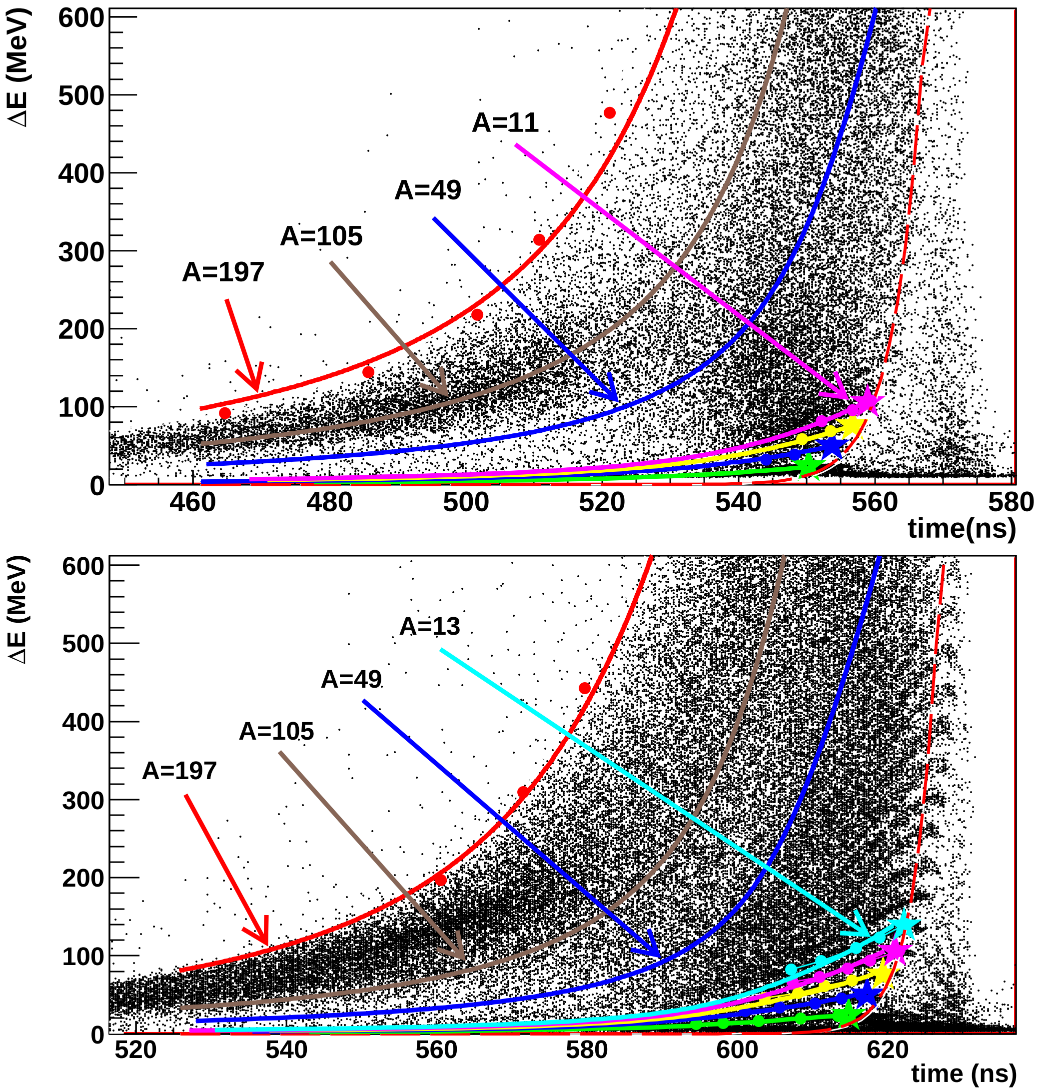

Figure 3.11: The $\Delta E - time$ distributions for detectors 404 (top panel) and 653 (bottom panel) located at $\theta = 17°$ and $28.5°$, respectively. Lines presented of both figures correspond to positions of masses as indicated.

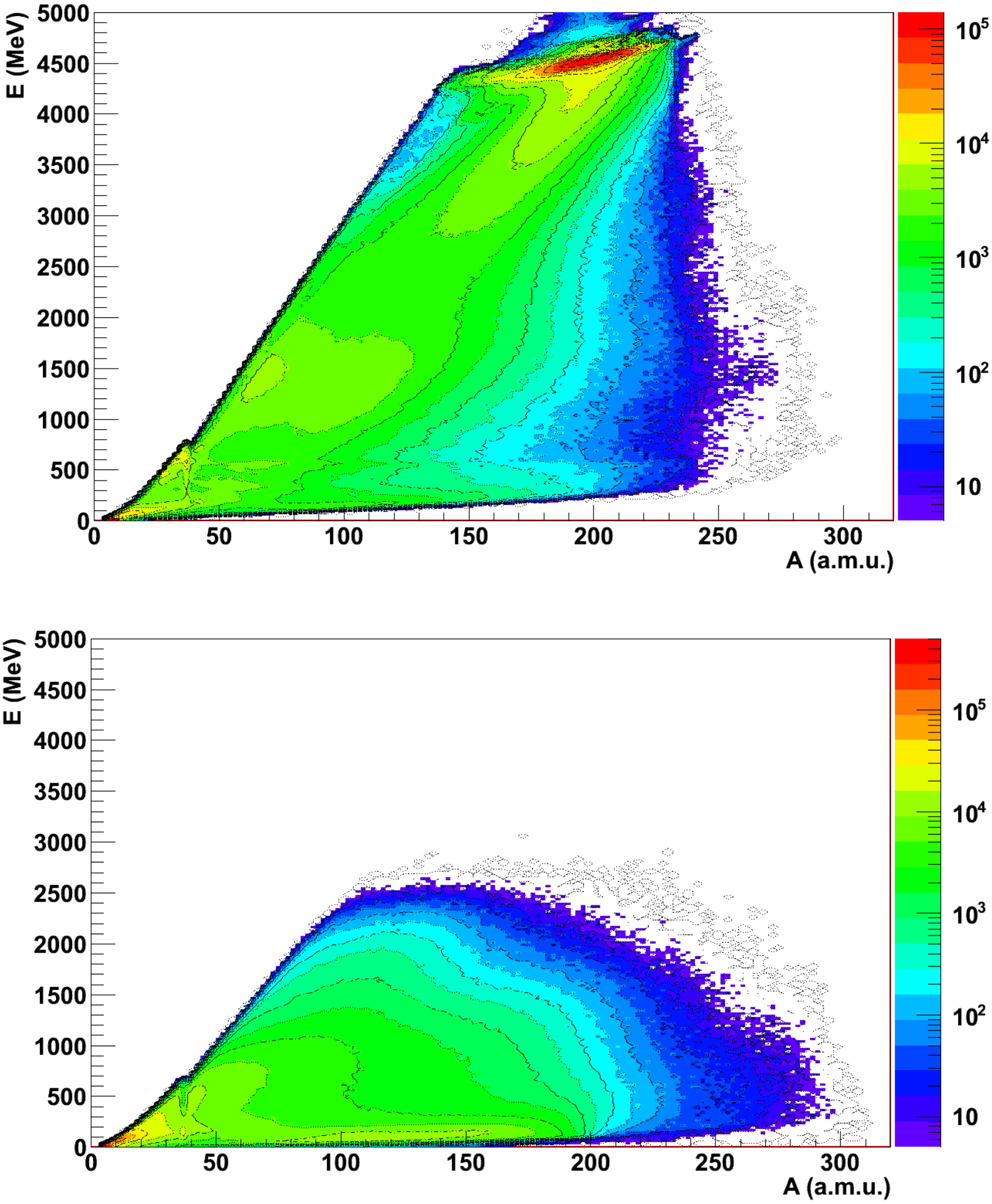

Figure 3.12: The correlation between mass and energy for fragments observed in telescopes located at $3^\circ < \theta < 10^\circ$ and $20^\circ < \theta < 28.5^\circ$ (top and bottom panel, respectively).

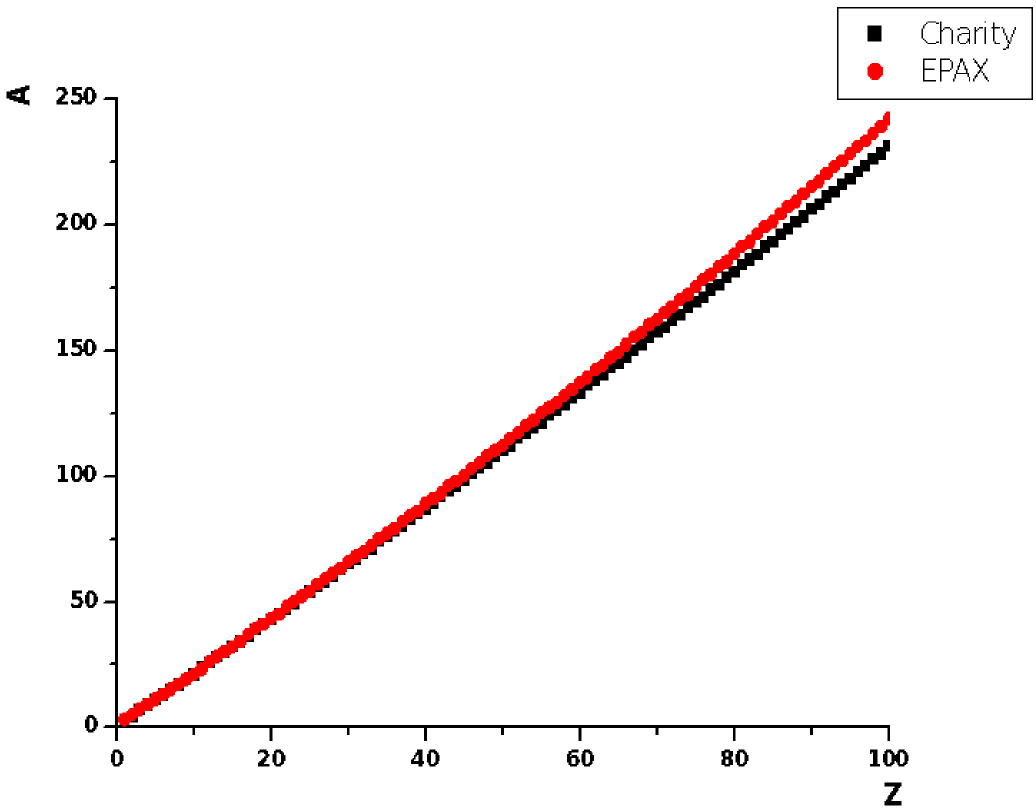

Figure 3.13: A(Z) dependence for Charity and EPAX2 formulas.

Chapter 4

Global data properties

In this chapter the research results of calibrated experimental data consistency have been shown.

First we present two-dimensional distribution mass versus parallel velocity of identified fragments (see Fig. 4.1). The location of quasielastic Au peak is visible at a mass around 200 and velocities close to the beam velocity ($v_p = 6.67\frac{cm}{ns}$). The peak corresponding to Au recoil fragment can be found at velocities close to zero. At velocities between these two limits fragments originating from fission of the Au-like nuclei are located. One can also identify a separated region located at low masses and velocity close to the center of mass velocity. This region corresponds to the intermediate velocity source.

For the identified fragments ($Z_{frag} \geq 3$) we have constructed the plot presenting the dependence between the total charge of identified fragments, Z_{tot}, versus total parallel momentum of those fragments normalized to the beam momentum, $p_{\parallel,tot}/p_{proj}$ (see Fig. 4.2). One can distinguish different regions on this plot. The region where both momentum and charge are close to 0 corresponds to badly identified events. In the region of total parallel momentum close to 1 and total collected charge close to the charge of the projectile one observes the maximum corresponding to deep inelastic collisions when the target-like fragment stays undetected. In the region where total parallel momentum is close to 0 and total collected charge is close to the charge of the target, we detected only a target-like fragment. The region where the total detected charge is close to the total charge of the system and the total parallel linear momentum is close to the linear momentum of the projectile can be called as the region of well defined events. In our present

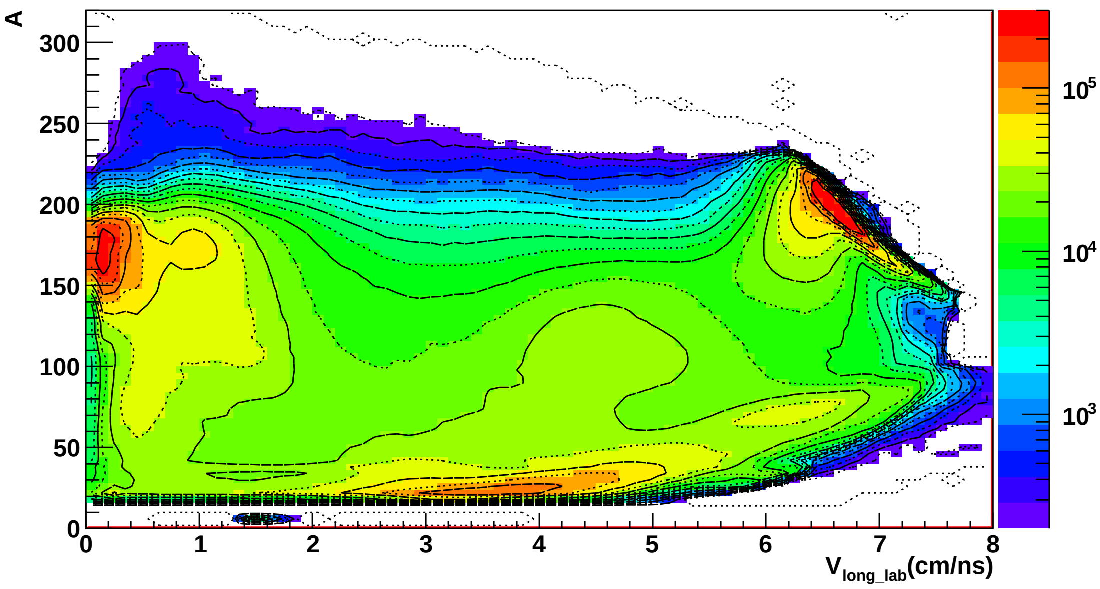

Figure 4.1: The correlation between the mass of identified fragments versus parallel velocity of those fragments.

analysis this region is delimited by the conditions:

$$120 < Z_{tot} < 180 \; and \; 0.8 < p_{\|,tot}/p_{proj} < 1.1. \tag{4.1}$$

For the class of well defined events in the $Au + Au$ reaction the multiplicity distributions of fragments with charge $Z_{frag} \geq 3$ and $Z_{frag} \geq 10$ are presented in Fig. 4.3. The number of events with 3, 4, and 5 or more fragments for two levels of thresholds are presented in Table 4.1.

N_{frag}	$Z_{frag} \geq 3$	$Z_{frag} \geq 10$
3	646 000	377 000
4	211 000	44 000
≥ 5	129 000	5000

Table 4.1: The multiplicity values for the class of well defined events.

One should expect that for $Au + Au$ system at relatively low interaction energy

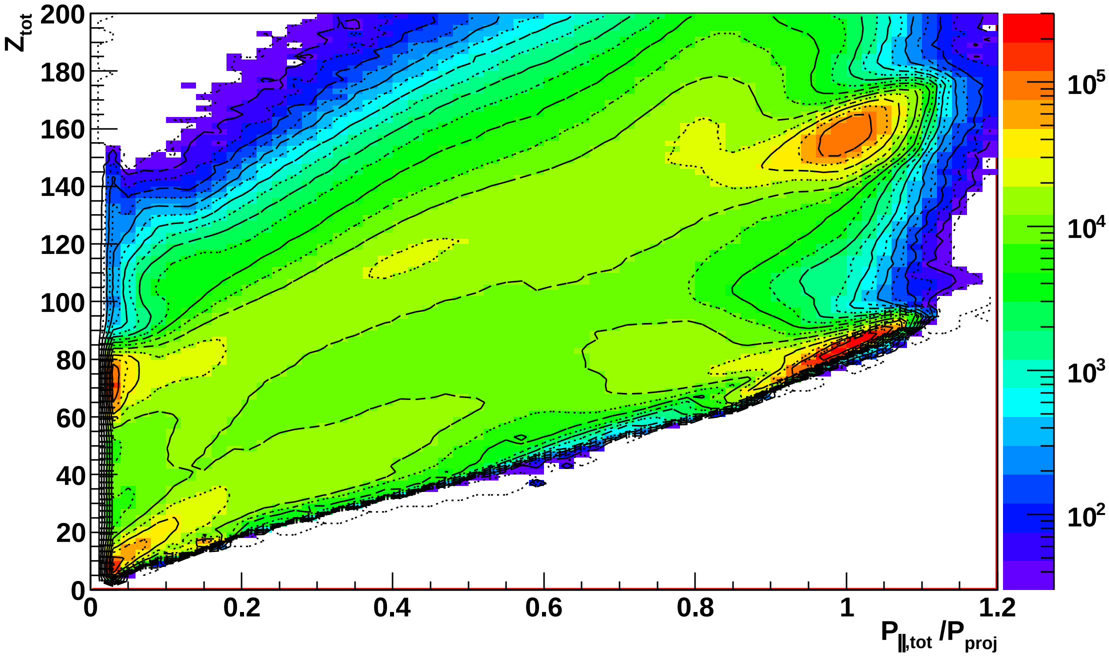

Figure 4.2: The correlation between the total charge of identified fragments, Z_{tot}, versus total parallel momentum of those fragments normalized to the beam momentum, $p_{\parallel,tot}/p_{proj}$.

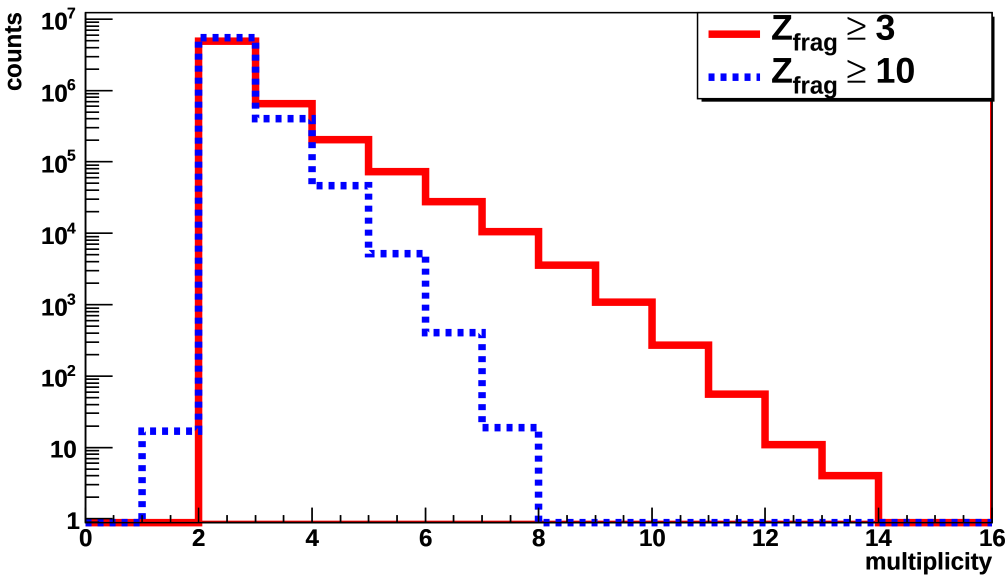

Figure 4.3: The number of events distributions of fragments with $Z_{frag} \geq 3$ (red histogram) and $Z_{frag} \geq 10$ (blue histogram), respectively.

the binary deep inelastic collisions will prevail, followed by fission of one (PLF - projectile-like fragment or TLF - target-like fragment) or two (PLF and TLF) interacting nuclei. As a result of such reaction scenario three or four heavy fragments will be formed.

In case of PLF nucleus fission in $^{197}Au+^{197}Au$ reaction the velocity distribution of fragments can be seen in Fig. 4.4. The fragments with mass greater than 130 and negative velocity in the center of mass frame of reference are treated as TLF. Additionally all fragments must have mass greater than 50. The reaction scenario can be written as:

$$^{197}Au+^{197}Au \rightarrow TLF+PLF \rightarrow TLF+F1+F2, \tag{4.2}$$

where F1 and F2 are fragments created in PLF fission. The PLF reconstruction results can be seen in Fig. 4.5.

The reaction scenario for fission of TLF and PLF nuclei is given as:

$$^{197}Au+^{197}Au \rightarrow TLF+PLF \rightarrow F1+F2+F3+F4, \tag{4.3}$$

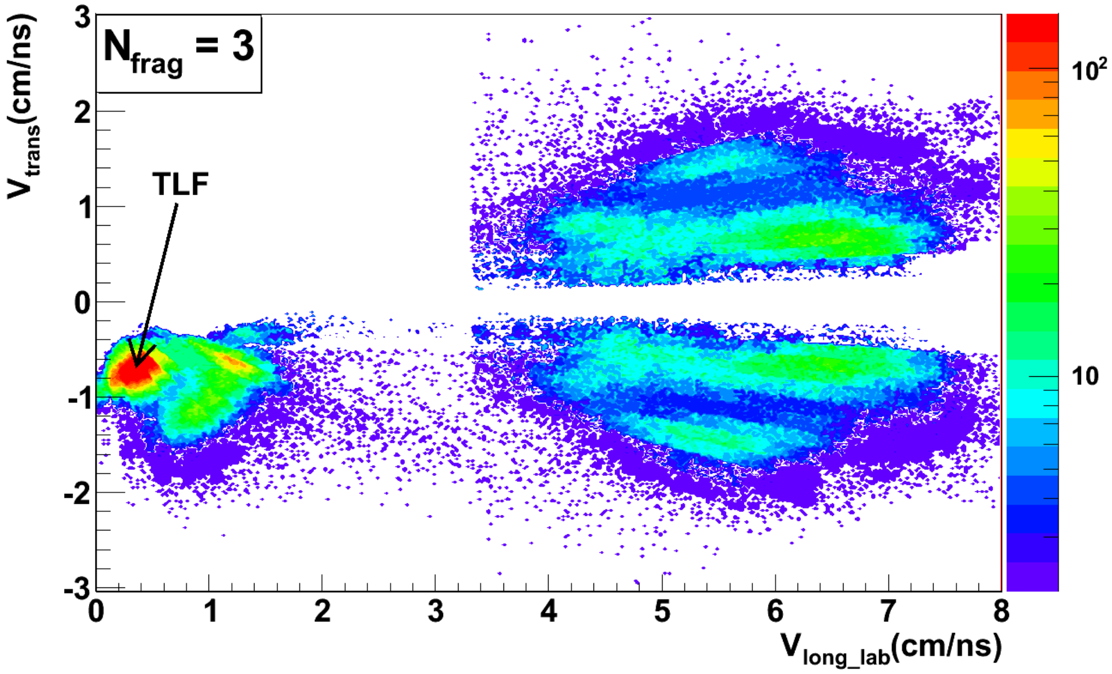

Figure 4.4: The invariant velocity distribution of TLF and the primary PLF reconstructed from two fission fragments. The plot was constructed for the class of events with three fragments requiring additionally that the TLF has mass greater than 130 and the lightest fragment has mass greater than 50.

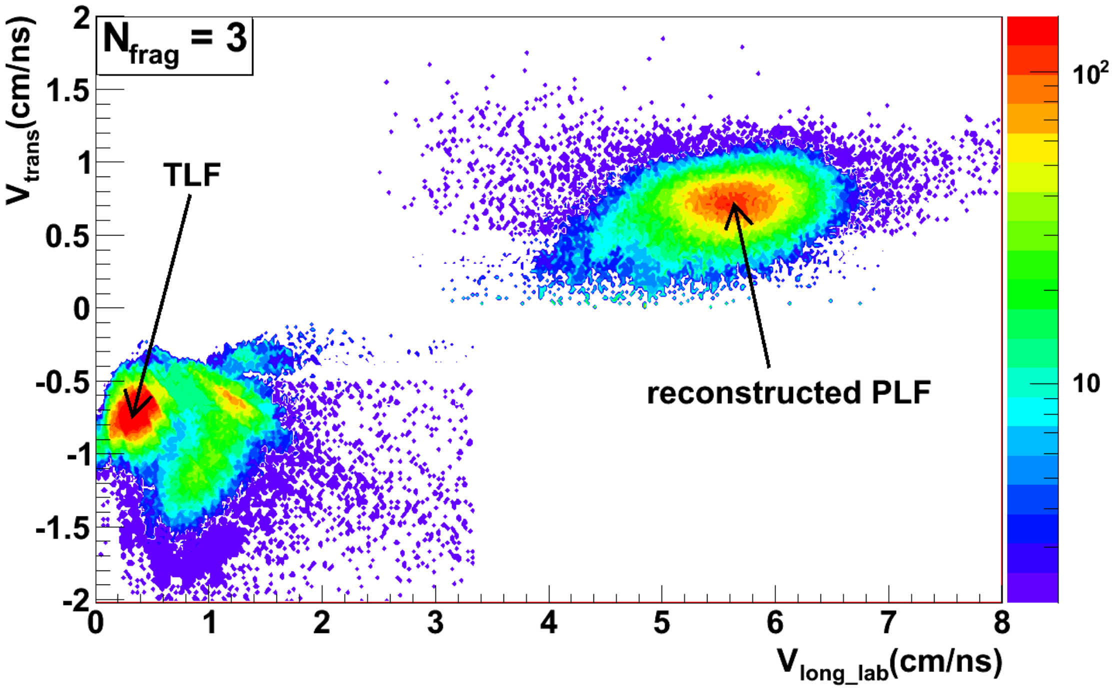

Figure 4.5: The invariant velocity distribution of TLF and the primary PLF reconstructed from two fission fragments. The plot was constructed with the same conditions as 4.4.

where F1, F2 and F3, F4 are fragments created in TLF and PLF fission, respectively.

The fragments with negative velocity in laboratory frame of reference are treated as originating from TLF decay, while the fragments with positive velocities are treated as originating from PLF. It was also required that all fragments must have mass greater than 50. The TLF and PLF reconstruction results can be seen in Fig. 4.6. Mass number distributions of the TLF and PLF for both reaction scenarios are shown in Fig. 4.7. Results of the dedicated analysis can be found in [35, 36].

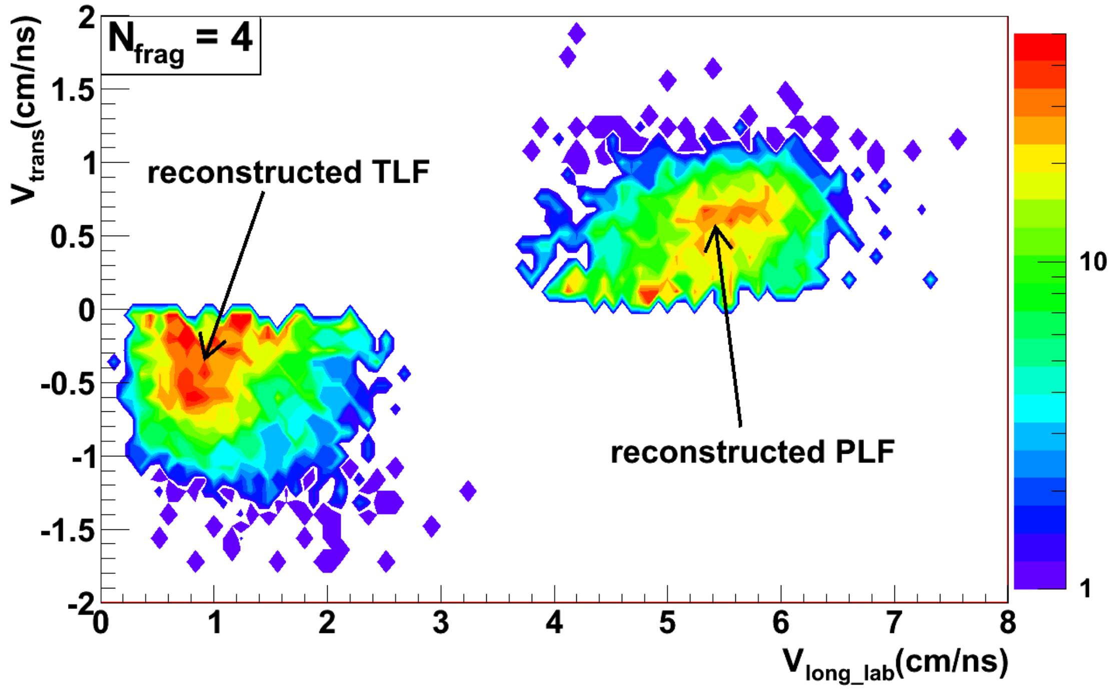

Figure 4.6: The invariant velocity distribution of reconstructed TLF and the PLF nuclei. The plot was constructed for the class of events with four fragments requiring additionally that the lightest fragment has mass greater than 50.

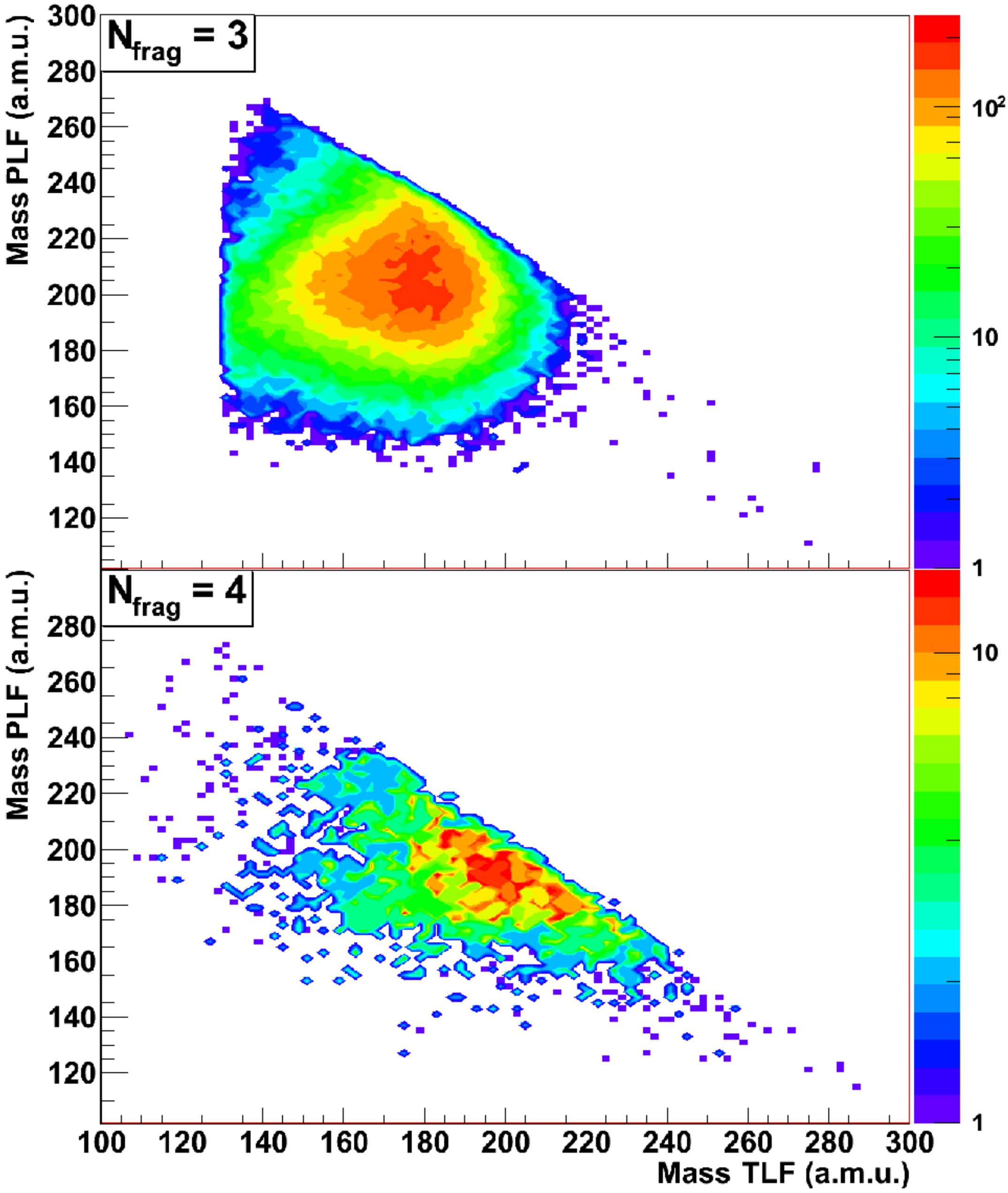

Figure 4.7: The mass number distributions of the TLF versus reconstructed PLF for reaction scenarios 4.2 and 4.3 (top and bottom panel, respectively). On the top figure TLF must have mass greater than 130 and negative velocity in the center of mass frame. On the bottom figure TLF must have negative velocity in the center of mass frame, while PLF must have positive velocity. In both cases all fragments must have masses greater than 50.

Chapter 5

Data analysis

The applied theoretical models have been presented in this chapter. The comparison results between experimental data and different models have been shown.

For the class of events with five fragments one can consider at least two mechanisms responsible for the presence of the fifth heavy fragment:

- creation of the fragment in the interaction region (intermediate velocity source - IVS) for more peripheral collisions;
- the multifragmentation of the composite nuclear system formed in central collisions.

In order to investigate the reaction scenario responsible for events with five fragments we have compared experimental data with ETNA (Expecting Toroidal Nuclear Agglomeration) [24] and QMD (Quantum Molecular Dynamics) [37] model predictions.

5.1 Theoretical models

5.1.1 ETNA model

The ETNA program allows to simulate the decay of nuclear systems with exotic shapes. It is assumed that for energies not higher than 15 AMeV, all the nucleons from the target and the projectile take part in the reaction. For higher energies some of them are emitted from the interaction region in the first reaction stage, before the equilibrium state is established [38]. The charge Z_{CN} and mass A_{CN} values of the created nuclear object are given:

$$\begin{aligned} Z_{CN} &= Z_T + Z_P - Z_{preq}, \\ A_{CN} &= A_T + A_P - A_{preq}, \end{aligned} \tag{5.1}$$

where Z_T is an atomic number of the target, Z_P is an atomic number of the projectile, Z_{preq} is a proton number emitted in the first reaction stage. A_T, A_P, A_{preq} are masses of the created nuclear system, target, projectile and emitted nucleons, respectively. The number of pre-equilibrium particles was estimated from the systematics presented in [38].

The number of created fragments N is given as an input variable. The fragments charges and masses are selected according to the Gaussian distribution. The maxima of the fragments charge and mass distributions are located at $\langle Z_{frag} \rangle = \frac{Z_{CN}}{N}$ and $\langle A_{frag} \rangle = \frac{A_{CN}}{N}$.

The ETNA model can simulate the decay of nuclear system assuming compact and non-compact freeze-out configurations. In the simulations the following freeze-out configuration shapes have been considered:

- ball geometry with volume 3 and 8 times larger than the normal nuclear volume (fragments uniformly distributed inside the sphere);
- fragments distributed on the surface of the sphere mentioned above (bubble configuration);
- fragments distributed on the ring with diameter 12 fm and 15 fm (toroidal configuration).

The ball freeze-out configuration size is consistent with the data analysis results for the reaction $Gd + U$ at energy of 36 AMeV [39]; the toroids sizes correspond to Warda calculation predictions [15]. For each configuration the fragments are placed randomly inside the freeze-out volume. In this configuration particles do not feel nuclear interaction and there are no nuclear reactions between them. If the condition $R_{ij} > R_i + R_j + 2fm$ is not met (fragments are overlapping) the case is rejected and the procedure is repeated. Here R_{ij} is the distance between fragments i and j and R_i, R_j are the radii of corresponding fragments).

The angular momentum of the system was corresponding to the entrance channel angular momentum related to impact parameter range from 0 to 3 fm. The available

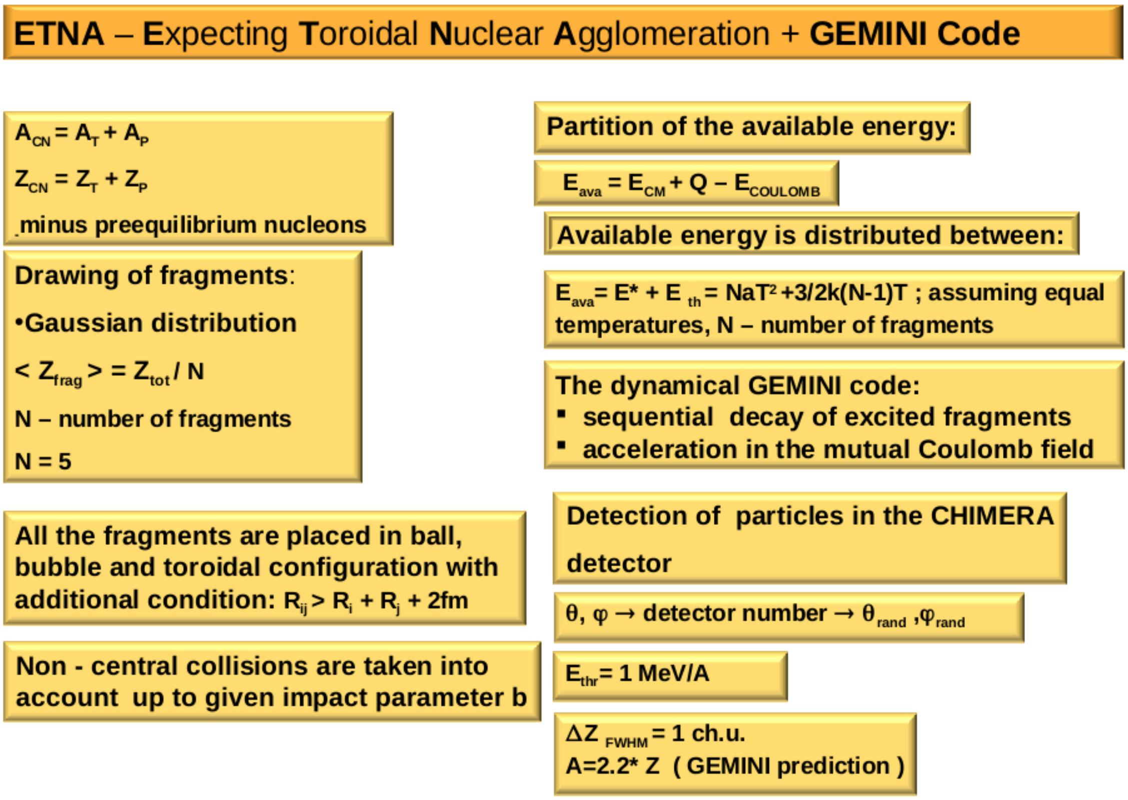

Figure 5.1: ETNA flow diagram.

energy for created systems is given:

$$E_{ava} = E_{CM} + Q - E_C, \tag{5.2}$$

where E_{CM} is the kinetic energy of the input channel in the mass center system, Q is the reaction heat and E_C is the Coulomb energy of the fragments placed at initial positions inside the freeze-out configuration. The available energy is distributed between the fragments excitation energy and their thermal motion energy, assuming the same temperature for thermal motion and internal excitation:

$$E_{ava} = \sum_{i}^{N} \frac{A_i}{8} T^2 + (N-1)\frac{3}{2} k_B T, \tag{5.3}$$

where: N is fragments number, A_i is the mass number of the i-th fragment and k_B is the Boltzmann constant. The first term refers to internal excitation, the second to thermal motion of the fragments.

The fragments are cooled and accelerated in the mutual Coulomb field, using the dynamical version of Gemini program [40]. The cool fragments are filtered by the software replica of CHIMERA detector [41]. There has been considered the detector granulation, the resolution at the level of 1 charge unit and the detection threshold of 1 AMeV have been assumed. The fragments' masses have been calculated from the formula: $A = 2.08Z$, which was in accordance to GEMINI calculations. The ETNA program flow diagram is shown in Fig. 5.1.

In this work there are presented results with additional assumption that the decay fragments number N equals to five. In ETNA model we consider only events corresponding to central collisions (0-3 fm impact range).

5.1.2 QMD model

The QMD model simulates heavy ion reactions preserving multi-body correlations and fluctuations. Each nucleon within the model is represented by a wave packet, given by a wavefunction with time-constant minimal wavefunction width:

$$\Psi_i(\vec{r}, t) = \frac{1}{(2\pi L)^{\frac{3}{4}}} e^{-\frac{(\vec{r} - \overrightarrow{r_{0i}}(t))^2}{4L}} e^{-\frac{i}{\hbar}\overrightarrow{p_{0i}}(t)\vec{r}}, \tag{5.4}$$

where $\overrightarrow{r_{0i}}$ and $\overrightarrow{p_{0i}}$ are position and momentum of the i-th nucleon in the described wave packet center respectively, while L represents the Gaussian width corresponding to the medium square radius of a nucleon ($1.8 fm^2$).

The wave packet width is constant, which is consistent with the observation that a cold nucleus radius is constant as well. The N-body wavefunction, describing the nucleus, is the product of N wavefunctions for single particles, which is a simplification violating the antisymmetricity of fermion wavefunction. The QMD model simulates the fermion effects using the effective Pauli potential where the final states for the individual nucleon-nucleon collisions are the subject of Pauli exclusion principle. The Pauli potential prevents the nucleons from being close together. The nucleons are randomly selected, then the overlapping condition is checked: when the distance between two nucleons is shorter than 1.5 fm, such an event is rejected. In the next step the local density around each nucleon is established and the local Fermi momentum $p_f^l = \hbar(\frac{3}{2}\pi^2\rho(\vec{r_i}))^{\frac{1}{3}}$ is calculated ($\rho(\vec{r_i})$ is a one-body density in real space). At the end, the nucleon momentum is randomly chosen in the interval $[0, \overrightarrow{p_f^l}]$. If two nucleons in the phase space are closer to each other than $d_{min} = (\vec{r_i} - \vec{r_j})^2 \cdot (\vec{p_i} - \vec{p_j})^2$, such a pair is rejected and the next random selection follows.

Such configurations are stable enough and nucleons do not leave the nucleus within the time of $300\frac{fm}{c}$. During the propagation the positions and momenta for the i-th nucleon are changed, whereas the wavefunction breadth remains the same. The system time evolution is given by the classical Hamilton equation for wave packets. The collision possibility for two nucleons is examined after each time step and the exclusion principle is considered, which makes the effective collision cross section decrease. Thus, whenever a collision occurs, the phase space for the final state is checked. If the collision is blocked, the momentum of nucleons scattered is the same, as the initial momentum. After a defined time the dynamical evolution is stopped. All nucleus which are separated in the configuration space by less than 3 fm are forming a cluster with specific charge, mass, position, momentum, binding energy, temperature, and spin.

The QMD model allows for such projectile energies, by which not more than 84% of all collisions are blocked. Hence, the lower limit of kinetic energy, where the QMD model is applicable, is $E_{kin}^{lab} = 20AMeV$. The cool fragments are filtered by the software replica of CHIMERA detector (the same way as in ETNA model). In order to simulate the contribution from non-central collisions the QMD model calculations were performed in the full impact parameter range 0-12 fm.

5.2 Shape sensitive observables

The aim of this work is to investigate the possibility of formation of exotic freeze-out configurations in heavy ion collisions $^{197}Au +^{197} Au$ at the energy 23 AMeV. The verification of above-mentioned hypothesis is carried out using observables sensitive to the shape of the created nuclear systems. They have been applied for experimental data and models predictions.

Many observables were proposed to distinguish shapes of studied objects. The sensitivity of these observables to the shape of freeze-out configurations of the ETNA and QMD models was investigated [24]. As more suitable there were chosen two observables proposed in Sochocka's PhD thesis: δ and Δ^2 [42]. Their construction was based on heavy fragments created in the freeze-out volume. In our analysis we used events in which there have been at least five such fragments.

The first observable - δ - describes the shape of event in momentum space. In this case we use the sphericity (sph) and coplanarity (cop) variables [43]. Their definition is based on the momentum tensor:

$$F_{ij} = \frac{\sum_{n=1}^{N_{frag}} \frac{p_{i,n} p_{j,n}}{|\vec{p_n}|}}{\sum_n |\vec{p_n}|}, \tag{5.5}$$

where N_{frag} is the number of fragments in event, $p_{i,n}$ is the i-th component of the momentum of the n-th fragment, $\vec{p_n}$ is the momentum vector of the n-th fragment. The diagonalization of the momentum tensor gives the eigenvalues: t_i, $(t_1 < t_2 < t_3)$. For ordered eigenvalues of the tensor F one defines the reduced quantities:

$$q_i = \frac{t_i^2}{\sum_j t_j^2}. \tag{5.6}$$

Then sphericity and coplanarity are defined:

$$sph = \frac{3}{2}(1 - q_3), \tag{5.7}$$

$$cop = \frac{\sqrt{3}}{2}(q_2 - q_1). \tag{5.8}$$

In relation with sph and cop we define the θ_{flow} angle (see Fig. 5.2) as the angle between the beam axis and the eigenvector $\overrightarrow{e_1}$ for the largest eigenvalue λ_1.

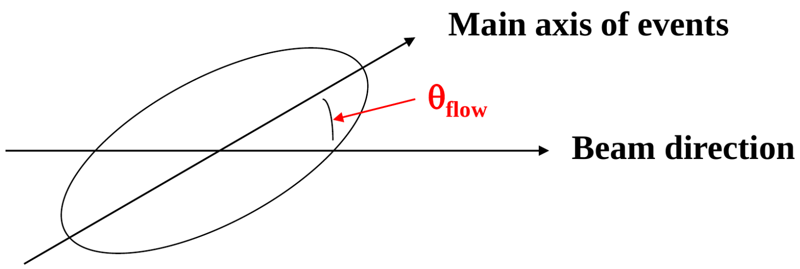

Figure 5.2: θ_{flow} angle definition.

In the (sph, cop) plane (see Fig. 5.3) all events are located inside a triangle defined by points (0, 0), ($\frac{3}{4}$, $\frac{\sqrt{3}}{4}$), (1, 0). In the case of ball and bubble geometries the maxima of the corresponding distributions are located in the center of the triangle. For toroidal configurations the distributions are located closer to the line (0, 0), ($\frac{3}{4}$, $\frac{\sqrt{3}}{4}$). In Fig. 5.4 the distributions of events in the (sph, cop) plane for experimental data and different freeze-out configurations was shown. The variable δ measures the distance between the given point in the (sph, cop) plane and above the line:

$$\delta = \frac{1}{2}|-sph + 1.732cop|. \tag{5.9}$$

In Fig. 5.5 (left panels) the δ variable distribution for different freeze-out configurations was shown. One can see here that the δ distribution for experimental data is similar to that corresponding to QMD predictions. The biggest difference can be observed with the distribution for Ball $8V_0$ configuration.

The second variable - Δ^2 - used in our analysis measures the flatness of events in the velocity space. For each event we establish the plane in the velocity space (see Fig. 5.6). The parameters of this plane are selected in the way that the sum of squares of distances between the plane and the endpoints $(v_{x,i}, vy, i, v_{z,i})$ of velocity vectors reaches the minimum value. This quantity is defined as:

$$\Delta^2 = min[\sum_{i=1}^{5} d_i^2(A, B, C, D)], \tag{5.10}$$

where:

$$d_i = \frac{A \cdot v_{x,i} + B \cdot v_{y,i} + C \cdot v_{z,i} + D}{\sqrt{A^2 + B^2 + C^2}}. \tag{5.11}$$

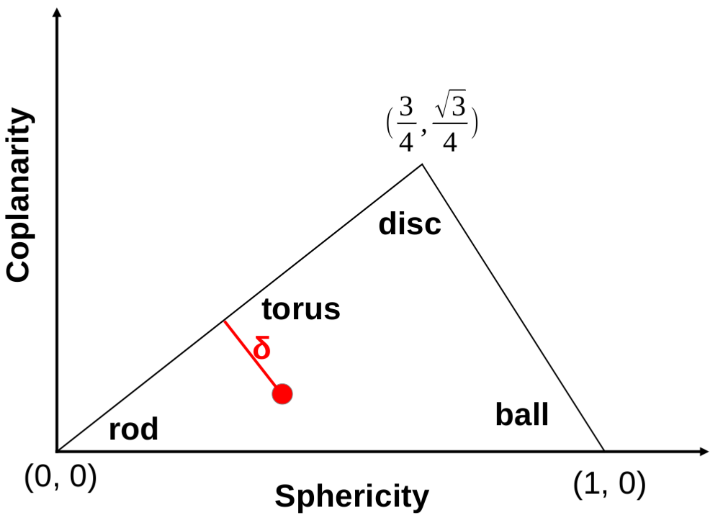

Figure 5.3: δ parameter definition.

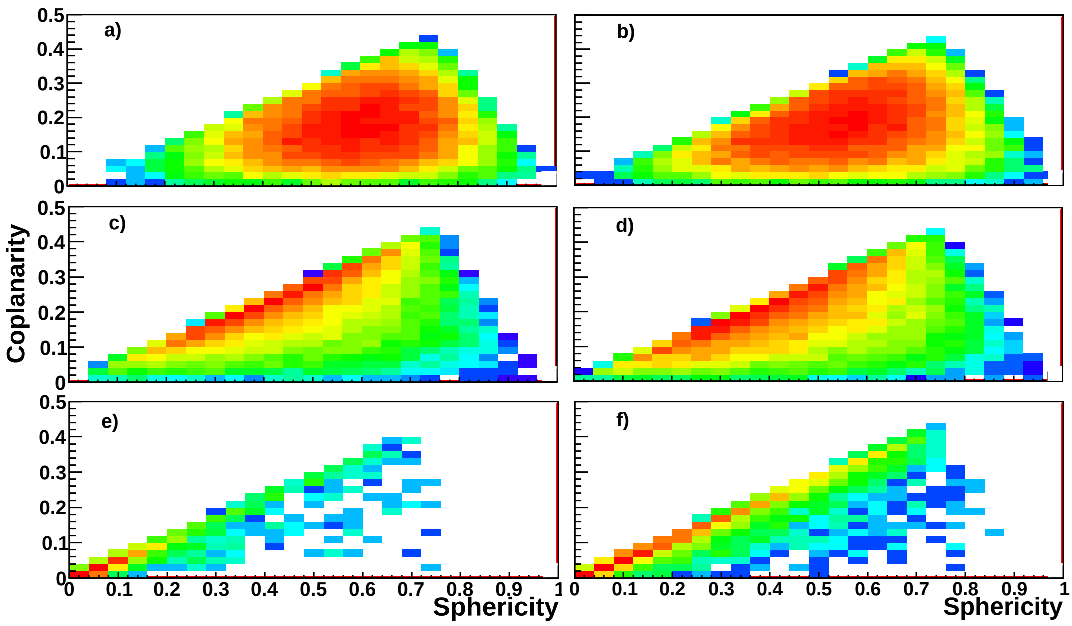

Figure 5.4: The sphericity - coplanarity distributions for $^{197}Au +^{197} Au$ collision at the energy 23 AMeV for: a) Ball $8V_0$, b) Bubble $8V_0$, c) Toroid 12 fm, d) Toroid 15 fm, e) QMD and f) experimental data.

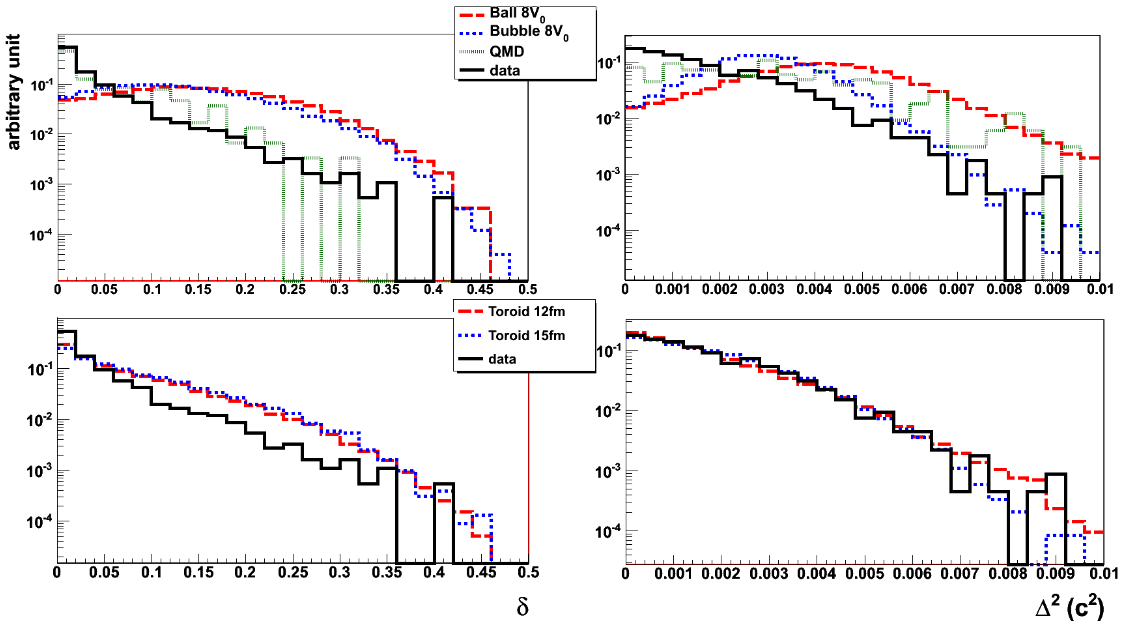

Figure 5.5: The δ distributions (upper left panel) are presented for experimental data, Ball $8V_0$, Bubble $8V_0$ freeze-out geometries and QMD predictions. In the bottom left panel the experimental distribution is compared with predictions for Toroid 12 fm and Toroid 15 fm configurations. In the right panels the Δ^2 distributions for experimental data and model predictions are shown. All the distributions presented here are constructed using the conditions: $Z_{frag} \geq 10$ and $\theta_{flow} > 20°$.

The parameters A, B, C, D are the plane parameters and the velocities of fragments are in the velocity of light units.

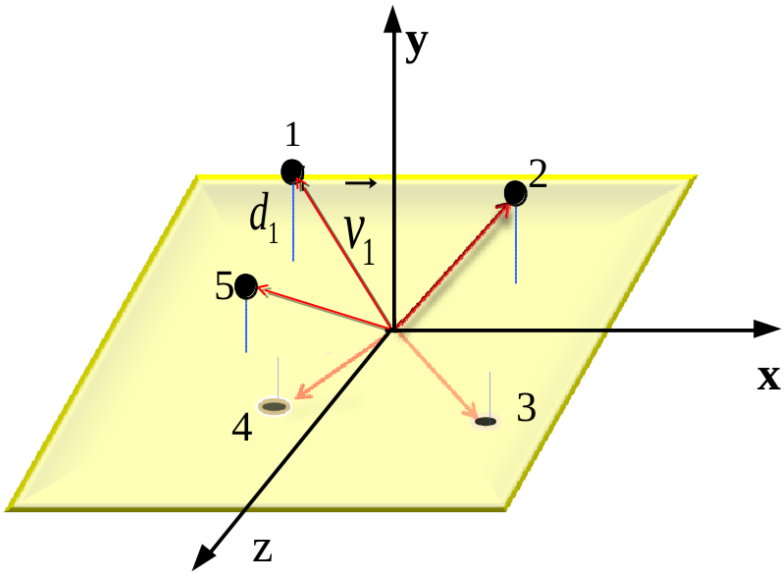

Figure 5.6: Δ^2 parameter definition.

The corresponding distributions are shown in Fig. 5.5 (right panels) for data and model predictions. One can see here that for Δ^2 variable the biggest difference between experimental distribution and model predictions is observed for the Ball $8V_0$ and Bubble $8V_0$ configurations.

In connection with Δ^2 parameter one can define an angle, θ_{plane}, between the beam direction and vector normal to the plane defined by parameters A, B, C, and D (see Fig. 5.7). For events corresponding to non-central collisions, where most of reaction products are located in the reaction plane, θ_{plane} should be close to 90°. For toroidal freeze-out configurations predicted by BUU calculations this angle should be significantly smaller.

In order to reduce non-central contribution we have investigated for the QMD model predictions the dependence between θ_{flow} and impact parameter (see Fig. 5.8 (top panel)). One can see on this plot that non-central events are located at small θ_{flow} angle. The similar dependence is observed for experimental data between θ_{flow} and total transverse momentum, p_{trans} or total kinetic energy $E^{CM}_{kin,tot}$, used as impact parameter estimator (see Fig. 5.8 (middle and bottom panels)). In our analysis we decide to reduce contributions of non-central events both for experimental data and

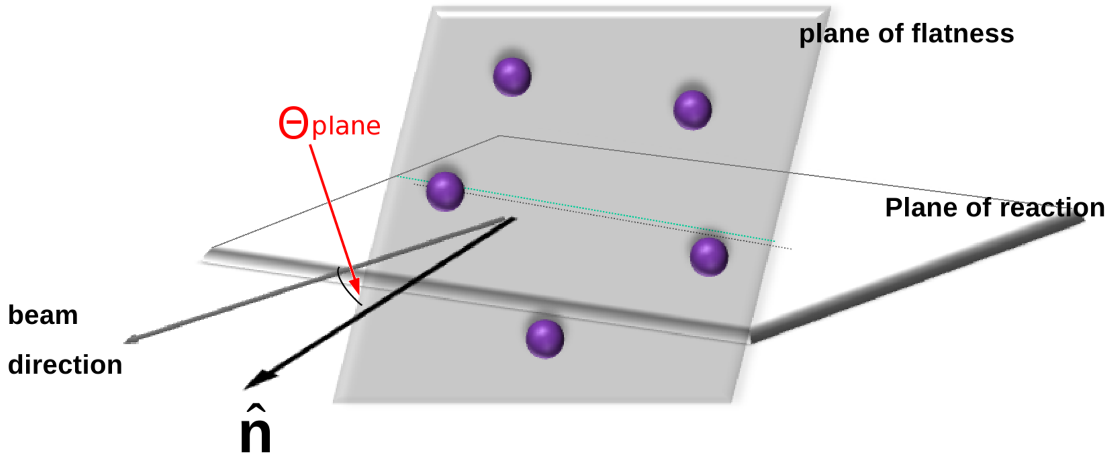

Figure 5.7: θ_{plane} angle definition.

model predictions by using the conditions: $\theta_{flow} > 20°$ [43].

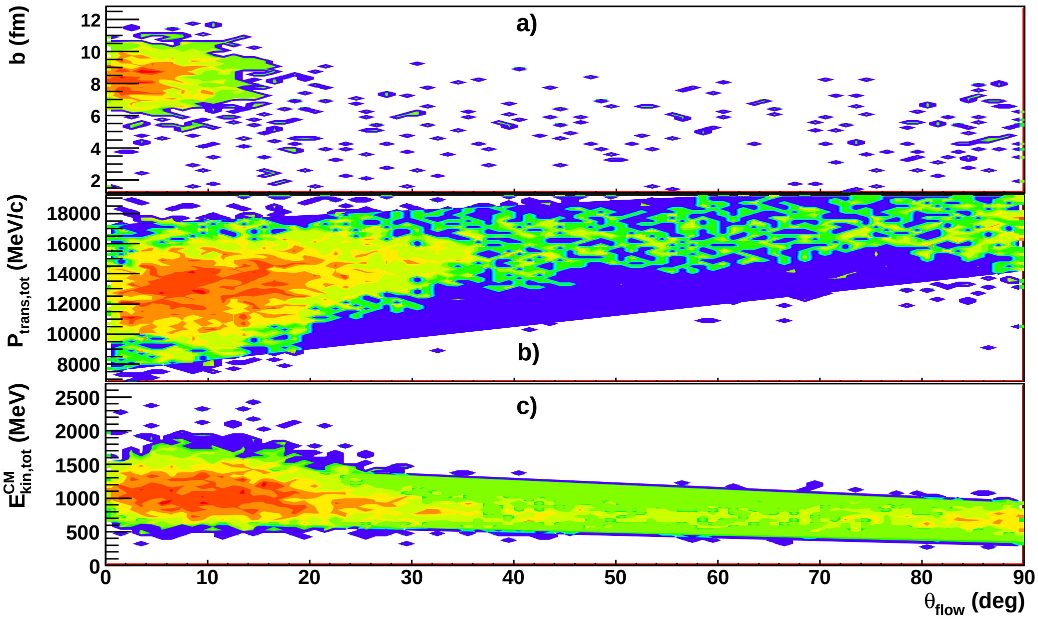

Figure 5.8: The impact parameter vs θ_{flow} dependence for QMD model predictions (top panel), p_{trans} momentum vs θ_{flow} and $E^{CM}_{kin,tot}$ energy vs θ_{flow} dependence for experimental data (middle and bottom panels). All the distributions presented here are constructed using the condition $Z_{frag} \geq 10$.

In order to reduce contribution of non-central collisions we also have investigated the dependence of θ_{plane} on the impact parameter (see Fig. 5.9 (top panel)). one can see that contrary to flow angle, non-central events are located at high θ_{plane} angles. Corresponding dependences between θ_{plane} and total transverse momentum, p_{trans} or total kinetic energy $E^{CM}_{kin,tot}$ are presented in Fig. 5.9 (middle and bottom panels). Additional condition: $\theta_{plane} < 75°$ is used.

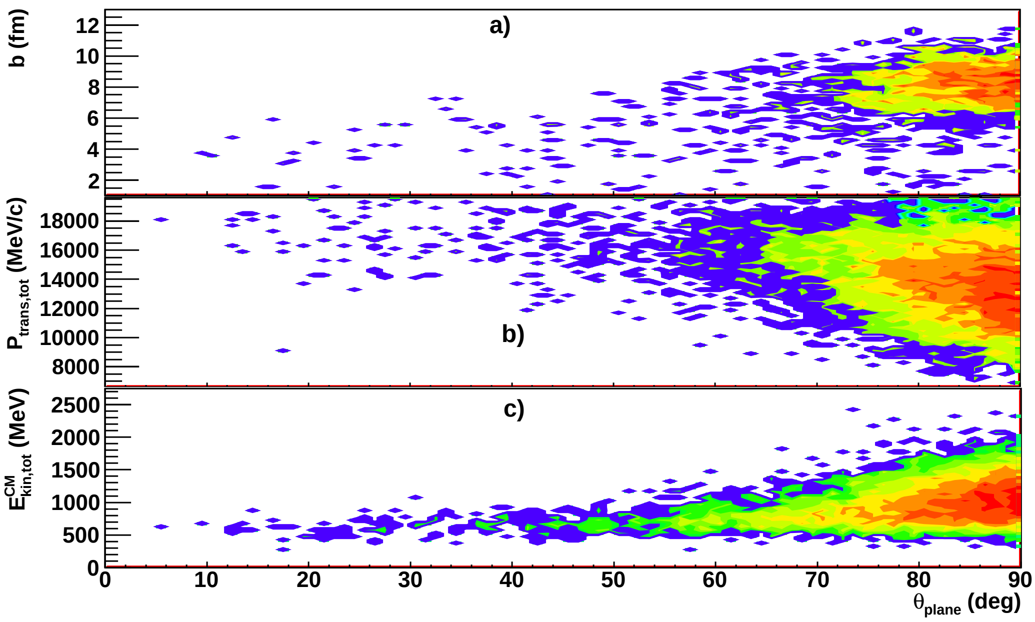

Figure 5.9: The impact parameter vs θ_{plane} dependence for QMD model predictions (top panel), p_{trans} momentum vs θ_{plane} and $E^{CM}_{kin,tot}$ energy vs θ_{plane} dependence for experimental data (middle and bottom panels). All the distributions presented here are constructed using the condition $Z_{frag} \geq 10$.

The dependence between θ_{plane} and θ_{flow} for Ball $8V_0$, Toroid 15 fm, QMD and experimental data is presented in Fig. 5.10. One can observe here that for experimental data most of events are located in the region selected by conditions $\theta_{flow} < 20°$ and $\theta_{plane} > 75°$. The same behavior is observed in the case of QMD calculations. These observations indicate that such events correspond to non-central collisions. For the Ball $8V_0$ configuration one observes the correlation between θ_{flow} and θ_{plane} angles. For toroidal configuration the correlation between these angles is even stronger. Most of these events are located in the region defined by conditions $\theta_{flow} > 20°$ and $\theta_{plane} < 75°$. In order to investigate a possible formation of toroidal configurations in our analysis we selected the region where according to the ETNA predictions for the toroidal configurations are located in the θ_{plane} vs θ_{flow} plane.

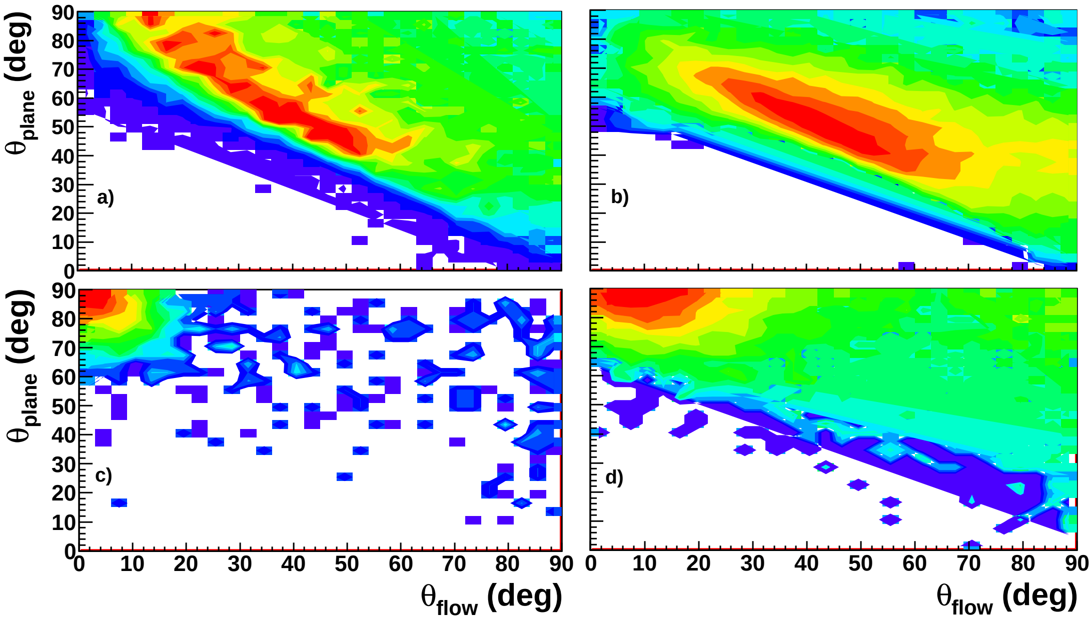

Figure 5.10: The dependence between θ_{plane} and θ_{flow} for: a) Ball $8V_0$, b) Toroid 15 fm, c) QMD, and d) experimental data. All the distributions presented here are constructed using the condition $Z_{frag} \geq 10$.

Following the method proposed in Ref. [24] we select events corresponding to the toroidal-shape by the set of conditions:

$$\Delta^2 < 0.001\ c^2 \ \textit{and} \ \delta < 0.05. \tag{5.12}$$

As an efficiency measure of the above conditions we take the ratio of number of events fulfilling the selection conditions to the number of events with five and more heavy fragments (EF, efficiency factor). The results of this procedure are presented in the Fig. 5.11 for different regions of θ_{flow} and θ_{plane} angles. As one can see the EF is very low for spherical freeze-out configurations with respect to the corresponding values for toroidal configurations. For QMD calculations the value of the efficiency factor is strongly dependent on the θ_{plane} range. For events selected by the condition $\theta_{flow} < 20°$ the EF drops to zero, when we consider events corresponding to small values of θ_{plane}. For experimental data the value of the efficiency factor is about 50% for events located in the reaction plane ($\theta_{plane} > 75°$) and is reduced by factor of 2 for events perpendicular to the reaction plane.

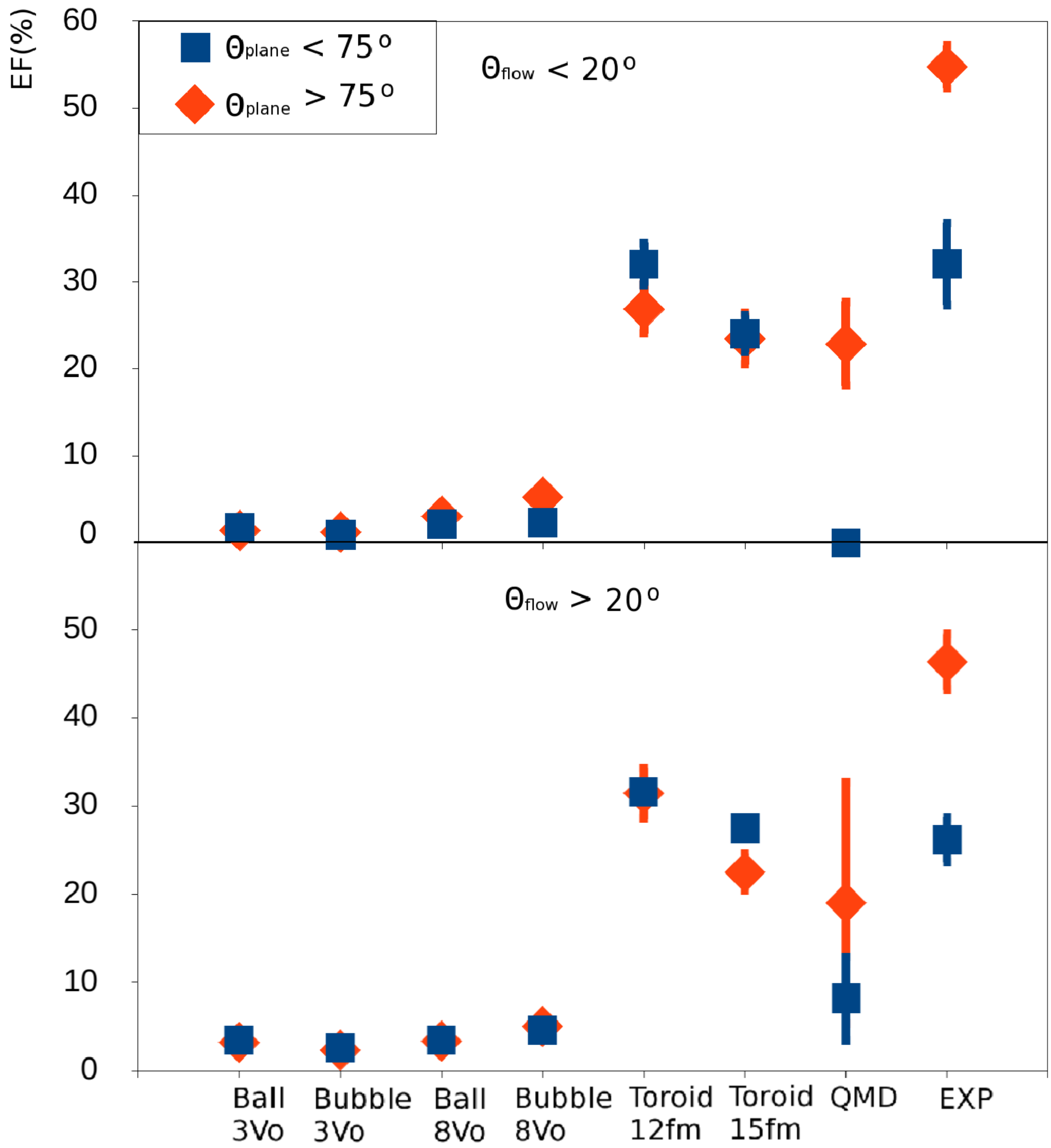

Figure 5.11: The EF values for different windows of θ_{plane} and θ_{flow}. The presented results were calculated using the condition $Z_{frag} \geq 10$.

In Table 5.1 the efficiency factor values are collected for experimental data and model predictions for a class of events selected by the conditions $\theta_{plane} < 75°$ and $\theta_{flow} > 20°$. The efficiency factor values are shown for four threshold values of the fragment charge.

Efficiency factor (%)				
Configuration	$Z_{frag} \geq 3$	$Z_{frag} \geq 10$	$Z_{frag} \geq 15$	$Z_{frag} \geq 20$
Ball $3V_0$	3.3 ± 0.2	3.5 ± 0.2	3.5 ± 0.2	3.5 ± 0.2
Bubble $3V_0$	2.4 ± 0.2	2.6 ± 0.2	2.7 ± 0.2	2.7 ± 0.2
Ball $8V_0$	3.2 ± 0.2	3.5 ± 0.2	3.5 ± 0.2	3.5 ± 0.2
Bubble $8V_0$	3.9 ± 0.2	4.6 ± 0.2	4.7 ± 0.2	4.7 ± 0.2
Toroid 12 fm	29.7 ± 0.6	31.6 ± 0.6	31.8 ± 0.6	31.9 ± 0.6
Toroid 15 fm	25.2 ± 0.5	27.5 ± 0.5	27.7 ± 0.5	27.8 ± 0.5
QMD	13.7 ± 3.4	8.2 ± 4.7	6.3 ± 5.5	N/A
data	27.1 ± 0.7	26.2 ± 2.5	26.2 ± 4.8	21.1 ± 8.0

Table 5.1: The efficiency factor at incident energy 23 AMeV for four threshold values of the fragment charge for events selected by conditions $\theta_{flow} > 20°$ and $\theta_{plane} < 75°$.

Here one can notice that the EF values for experimental data are very close to the model predictions for toroidal configurations. This observation may indicate the formation of toroidal/flat freeze-out configuration created in the $Au + Au$ collisions at 23 MeV/nucleon.

5.3 Other observables

In order to get additional evidence to support the hypothesis that toroidal objects are created, the behavior of other observables was investigated. We consider here for each event separately:

- mass standard deviations σ_A of fragments;
- relative velocities of fragments pairs (v_{ij});
- relative angles of fragment pairs (θ_{ij});
- mean velocities of fragments as a function of their mass.

First all these observables were constructed for events selected by conditions $\theta_{flow} > 20°$ and $\theta_{plane} < 75°$, where observation of toroidal freeze-out configurations is expected. Corresponding distributions are presented in Figs. 5.12, 5.13, 5.14, 5.15, respectively. The distributions of these observables were constructed for flat events selected by condition 5.12 (thick green histograms) and non-flat events (thin red histograms) selected by conditions:

$$\Delta^2 > 0.001\ c^2\ and\ \delta > 0.05. \tag{5.13}$$

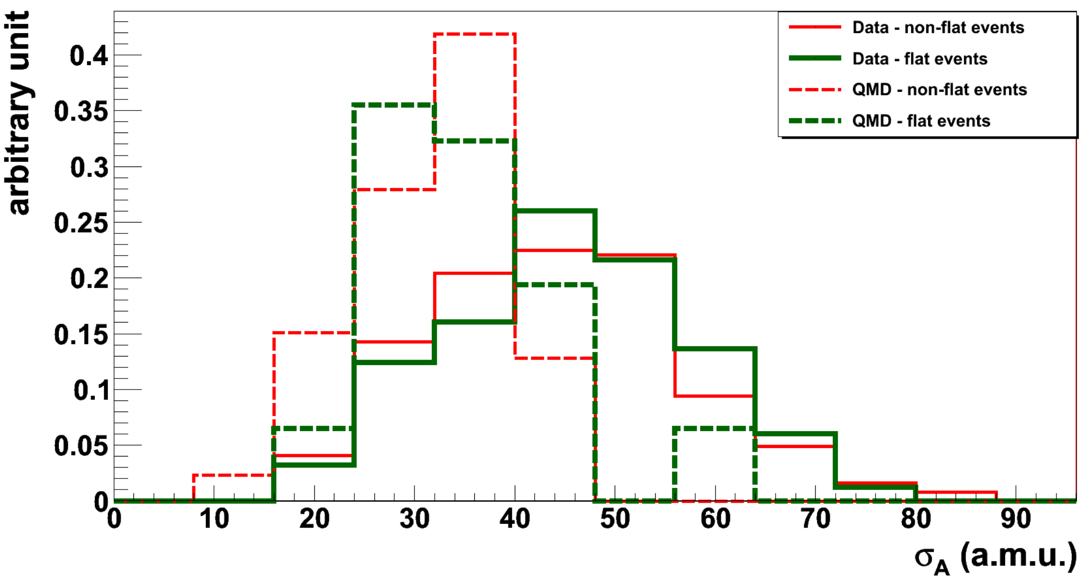

Figure 5.12: The distributions of standard deviation of the fragment mass for non-flat events (red lines) and flat events (green lines) for experimental data (solid lines) and QMD model predictions (dashed lines). All the distributions presented here are constructed using the condition $Z_{frag} \geq 10$.

Comparison of the σ_A distributions (Fig. 5.12) for flat and non-flat events indicates that in the case of flat events this distribution is slightly shifted to larger values. This observation is in contrast with the expectation that for the flat events the enhanced similarity in the size of fragments should be visible. The corresponding distributions for QMD calculations are similar (dashed lines). Their centroids are shifted to smaller values with respect to experimental data.

In Fig. 5.13 one observes that the distribution of relative velocities for flat events is shifted to smaller velocities in respect to non-flat events. The corresponding

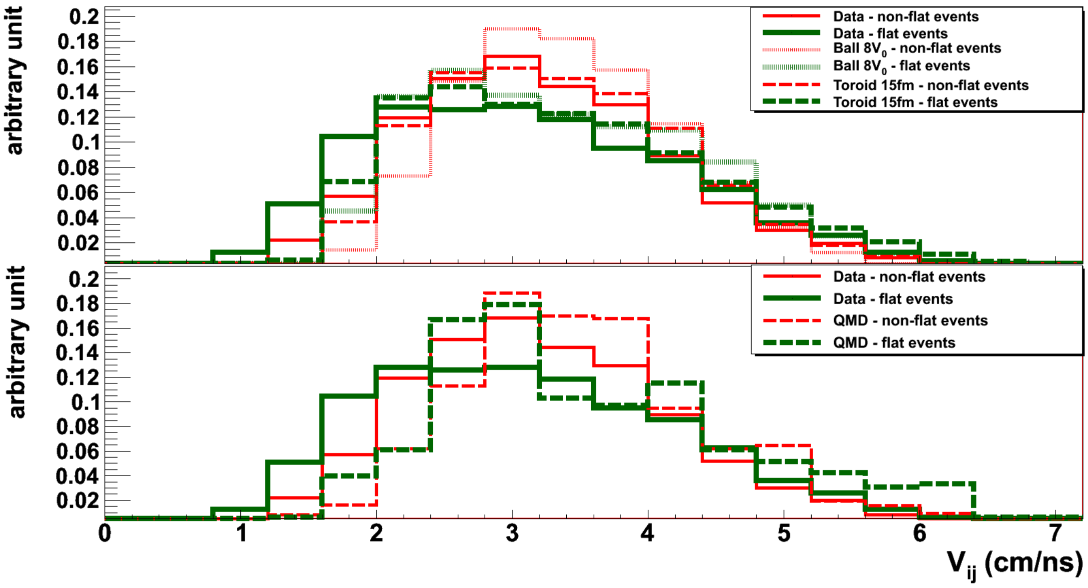

Figure 5.13: The distribution of relative velocities v_{ij} of fragments pairs for non-flat events (red lines) and flat events (green lines) for experimental data (solid lines) compared with: Ball $8V_0$, Toroid 15 fm (top panel), and QMD model predictions (bottom panel). All the distributions presented here are constructed using the condition $Z_{frag} \geq 10$.

distributions for Toroid 15 fm and Ball $8V_0$ ETNA model predictions show a similar dependence. This observation may indicate that the behavior of these v_{ij} distributions is insensitive to the shape of the freeze-out configuration.

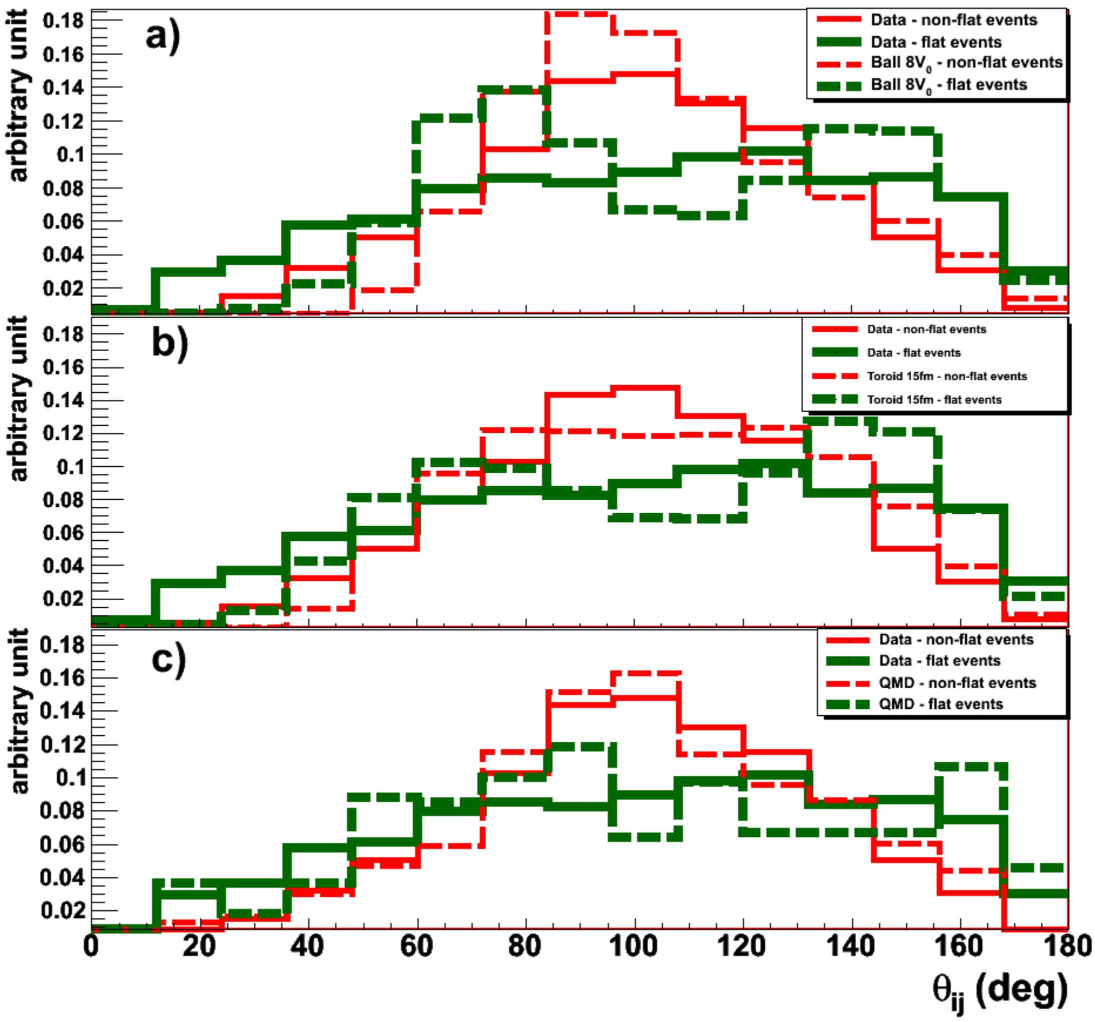

Figure 5.14: The distribution of relative angles θ_{ij} for fragment pairs for non-flat events (red lines) and flat events (green lines) for experimental data (solid lines) compared with: a) Ball $8V_0$, b) Toroid 15 fm, and c) QMD model predictions (dashed lines). All the distributions presented here are constructed using the condition $Z_{frag} \geq 10$.

Fig. 5.14 presents the distributions of relative angles θ_{ij} for fragment pairs. Here the experimental distributions for flat and non-flat events are compared with ETNA model predictions for Ball $8V_0$, Toroid 15 fm configurations, and QMD predictions.

For flat events the experimental distribution exhibits a broad plateau located around 90°. The same distribution for Ball $8V_0$ configuration shows two maxima located at 75° and 140°. Much weaker maxima are observed for Toroid 15 fm configuration. They are not visible in the QMD calculations.

The θ_{ij} distribution for non-flat experimental events shows a maximum located at 90°. The maximum for the Ball $8V_0$ configuration is even stronger. A similar dependence is observed for QMD results. For the Toroid 15 fm configuration the distribution is broader and similar to the experimental one.

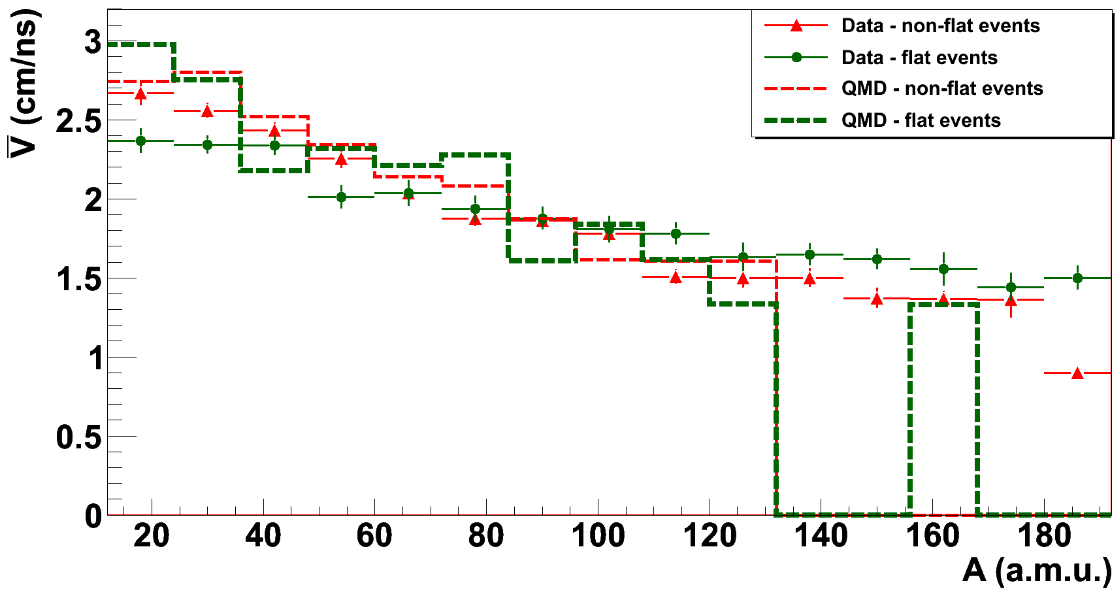

Figure 5.15: The distributions of mean velocities of fragments as a function of their mass for non-flat events (red lines) and flat events (green lines) for experimental data (points with error bars) and QMD model predictions (dashed lines). All the distributions presented here are constructed using the condition $Z_{frag} \geq 10$.

In Fig. 5.15 the distributions of mean velocities of fragments as a function of their mass for a flat and non-flat events are presented. On can observe that for flat events velocities of fragments decrease weaker with mass comparing to the same dependence for non-flat events. Comparison with same the dependences presented for Pb + Ag and Pb + Au systems at 29 AMeV [23] indicates that toroidal configurations may be created for some subclass of flat events.

Properties of flat events in the region where observation of toroidal freeze-out configurations is expected ($\theta_{flow} > 20°$ and $\theta_{plane} < 75°$) can be also compared with properties of flat events corresponding to other regions of θ_{flow} and θ_{plane} angles. Here the considered regions are the same as presented in Fig. 5.11. The distributions for σ_A of fragments and v_{ij} of for fragment pairs are presented in Fig. 5.16 using the condition $Z_{frag} \geq 10$. The mean values of σ_A and v_{ij} distributions are listed in Table 5.2. We can notice here that the corresponding mean values of the distribution of σ_A are similar for all θ_{flow} and θ_{flow} windows for a given threshold value of the fragment charge Z_{frag} (see Fig. 5.17 (top panel)). Such observation shows us that information carried by σ_A can not be used as a indication of toroidal objects formation. For v_{ij} distributions (see Fig. 5.17 (bottom panel)) one observes that the mean values for class of events located outside the reaction plane are smaller in comparison to the case of events located in the reaction plane. The smallest mean values are seen for the region where observation of toroidal freeze-out configurations are expected. This observation may be used as an indication that for events located outside the reaction plane freeze-out configuration is more extended in comparison with that for events located inside reaction plane.

Observable	threshold	$\theta_{flow} > 20°$ $\theta_{plane} < 75°$	$\theta_{flow} > 20°$ $\theta_{plane} > 75°$	$\theta_{flow} < 20°$ $\theta_{plane} < 75°$	$\theta_{flow} < 20°$ $\theta_{plane} > 75°$
$\sigma_A(a.m.u.)$	$Z_{frag} \geq 3$	72.09 ±0.47	71.09 ±0.35	76.43±0.52	73.33±0.13
	$Z_{frag} \geq 10$	47.01 ±1.88	47.15 ±1.33	46.41 ±2.68	45.06 ±0.58
	$Z_{frag} \geq 15$	38.31 ±2.98	38.53 ±1.24	35.24 ±5.11	35.58 ±0.98
	$Z_{frag} \geq 20$	31.01±6.68	31.10 ±2.60	25.15 ±5.15	27.17 ±1.59
	$Z_{frag} \geq 25$	17.51±5.07	18.95 ±5.86	20.94 ±4.82	18.50 ±2.23
$v_{ij}(cm/ns)$	$Z_{frag} \geq 3$	3.01 ±0.01	3.17 ±0.01	3.27 ±0.02	3.36 ±0.01
	$Z_{frag} \geq 10$	3.13 ±0.05	3.30±0.03	3.30 ±0.08	3.51 ±0.02
	$Z_{frag} \geq 15$	3.16 ±0.08	3.27 ±0.05	3.27 ±0.15	3.49 ±0.04
	$Z_{frag} \geq 20$	3.14 ±0.24	3.25±0.11	3.24 ±0.52	3.50 ±0.06
	$Z_{frag} \geq 25$	2.98 ±0.31	3.28 ±0.33	3.26 ±0.81	3.46 ±0.13

Table 5.2: The mean values of mass standard deviation of the fragments and of relative velocities v_{ij} of fragments pairs for flat events located in different windows of θ_{flow} and θ_{plane} angles.

Results obtained for the considered observables suggest that the formation of toroidal configurations can be related to a fraction of flat events tilted with respect to the reaction plane ($\theta_{plane} < 75°$). The probability for these events is much greater than the prediction of the QMD model. The nature of these events should be

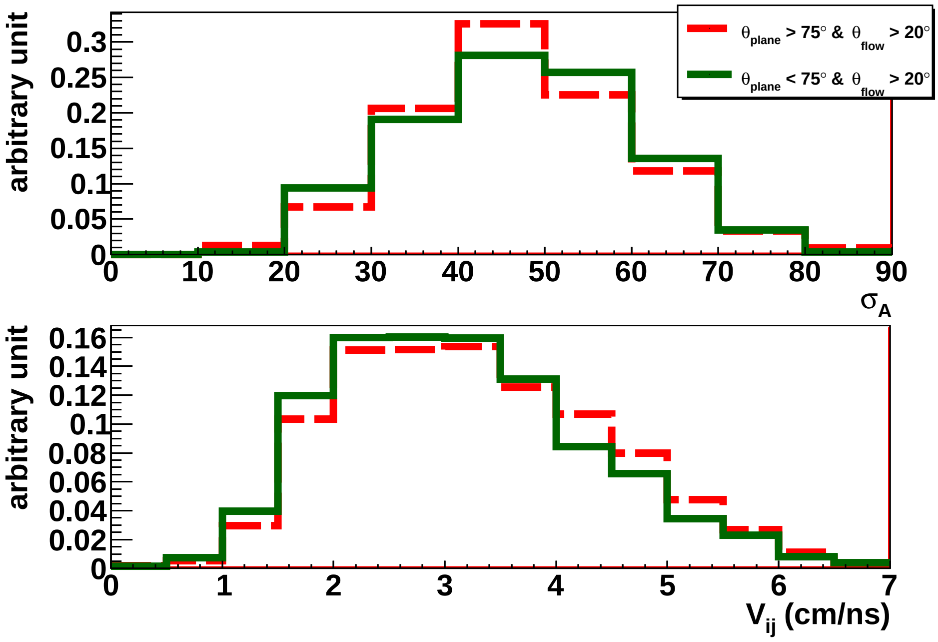

Figure 5.16: The distributions of standard deviation of the fragment mass (upper panel) and the distributions of relative velocities v_{ij} of fragments pairs (bottom panel) for flat events. The red dashed lines corresponds to events located inside the reaction plane and the green solid lines correspond to events located outside the reaction plane. All the distributions presented here are constructed using the condition $Z_{frag} \geq 10$.

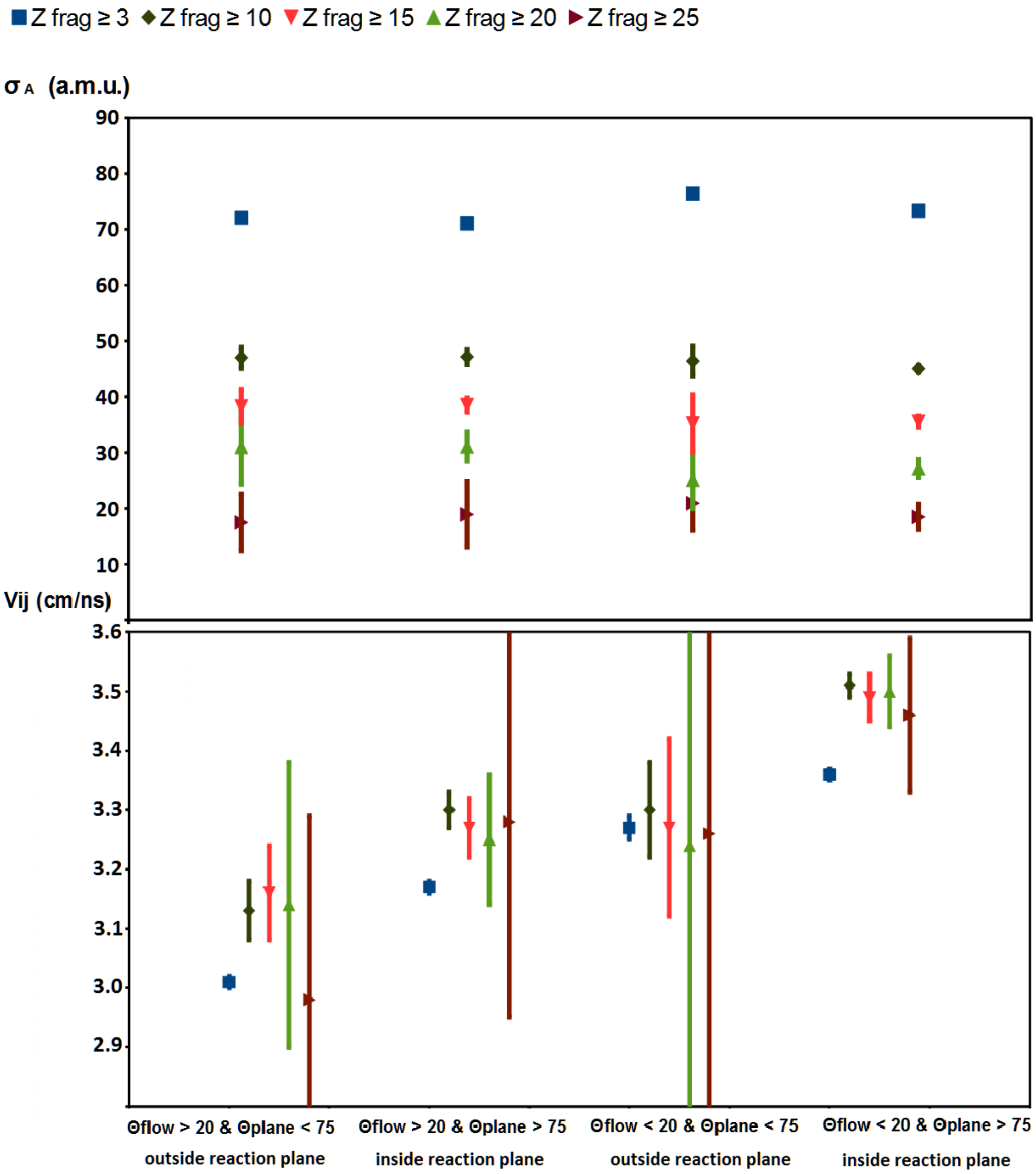

Figure 5.17: The distribution of mean values of mass standard deviation of the fragments (top panel) and of relative velocities v_{ij} of fragments pairs (bottom panel) in different windows of θ_{flow} and θ_{plane} angles for a given threshold value of the fragment charge.

investigated.

Assuming that the total number of detected events corresponds to 80% of total reaction cross section, the cross section related to creation of flat tilted events located in the region where observation of toroidal freeze-out configurations is expected can be estimated to be equal $17\mu b$.

Chapter 6

Summary

In this dissertation the possibility of creation of toroidal-shape freeze-out configurations in $^{197}Au +^{197} Au$ reaction at 23 AMeV has been investigated using CHIMERA 4π multidetector. In this work the information about particles was obtained using $\Delta E - E$ and ToF methods from over 1000 detection cells covering the polar angle from 3.1° to 130° and full range (2π) of azimuthal angle. The long and complicated energy, charge, and mass calibration procedures for all detectors were conducted.

There was selected the class of complete events for which the total charge of identified fragments is close to the total charge of the system and the total parallel linear momentum is close to the linear momentum of the projectile. There was investigated the reaction scenario for the multifragmentation of the composite nuclear system formed in central collisions. The events with five or more fragments were chosen for further analysis.

The experimental data were compared with statical and dynamical theoretical predictions using ETNA and QMD models. The novel shape sensitive observables: δ and Δ^2 were used to determine the shape of created nuclear systems. Additionally, in the connection with above mentioned observables two angles were defined: θ_{flow} and θ_{plane}, respectively. The dependence between θ_{flow}, θ_{plane} and impact parameter in QMD model predictions were used to reduce contribution of non-central collisions.

The possibility of formation of toroidal-shape nuclei was demonstrated by the efficiency factor. The efficiency factor for Ball $8V_0$, Bubble $8V_0$, Toroid 12 fm, Toroid 15 fm and QMD was calculated and compared with that for experimental data. Proximity of efficiency factor values for experimental data and toroidal freeze-out configurations may be used as an indication of the formation of an exotic freeze-out configuration. The juxtaposition of the standard deviation of fragment mass values for class events located outside and inside the reaction do not support the hypothesis of toroidal freeze-out configuration formation. Comparison of distributions of relative velocities for event with different orientation in respect to reaction plane gives evidence that the freeze-out configuration is more extended for class events located outside reaction plane. The behavior of mean velocities of fragments as a function of their mass for flat and non-flat events gives an indication that toroidal configuration may be created for some subclass of flat events. The probability of appearance of this flat events is much greater than the prediction of the QMD model. The nature of flat events tilted with respect to the reaction plane should be investigated. The related analysis is in progress.

Bibliography

[1] P.H.Abelson E.M.McMillan. *Phys.Rev.57, 1185*, 1940.

[2] G.T.Seaborg et al. *Phys.Rev.69, 366*, 1946.

[3] Z.Majka et al. *Acta Phys.Pol.B45, 279*, 2014.

[4] A.Marinov et al. *Int.J.Mod.Phys.E19, 131*, 2010.

[5] F.Dellinger et al. *Phys.Rev.C83, 065806*, 2011.

[6] A.Marinov et al. *Int.J.Mod.Phys.E20, 2403*, 2011.

[7] J.Decharge et al. *Nucl.Phys.A 716,55*, 2003.

[8] J.A.Wheeler. *Nucleonic Notebook, unpublished*, 1950.

[9] J.A.Wheeler R.E.Euwema. *unpublished*.

[10] H.Bethe P.J Siemens. *Phys.Rev.Lett 18, 704*, 1967.

[11] C.Y Wong. *Phys.Rev.Lett 55, 1973*, 1985.

[12] L.G Moretto et al. *Phys.Rev.Lett.78, 824*, 1997.

[13] G.Royer C.Fauchard. *Nucl.Phys.A598, 125*, 1996.

[14] K.Pomorski K.Dietrich. *Phys.Rev.Let.80, 37*, 1998.

[15] M.Warda. *Int.J.Mod.Phys.E16, 452*, 2007.

[16] C.Ngo S.R.Souza. *Phys.Rev.C48, R2555*, 1993.

[17] R.Adams et al. *Appl.Phys.39, 5173*, 1968.

[18] Kuo-Long Pan et al. *Phys.Rev.E80, 036301*, 2009.

[19] W.Bauer et al. *Phys.Rev.Lett.69, 1888*, 1992.

[20] H.M.Xu et al. *Phys.Rev.C48, 933*, 1993.

[21] C.Y.Wong. *Ann.Phys.(N.Y.) 77, 279*, 1973.

[22] N.T.B.Stone et al. *Phys.Rev.Lett.78, 2084*, 1997.

[23] B.Jouault et al. *Nucl.Phys.A 615, 82*, 1997.

[24] A.Sochocka et al. *Acta Phys.Pol.B40, 747*, 2009.

[25] A.Pagano et al. *Nucl.Phys.A734, 504*, 2004.

[26] P.Russotto. *PhD Thesis, Universita Degli Studi di Catania*, 2006.

[27] G.Pasaquali et al. *Nucl.Instr.Meth.A405, 39*, 1998.

[28] G.Tabacaru et al. *Nucl.Instr.Meth.A428, 379*, 1999.

[29] W.Gawlikowicz et al. *NIM.A491, 181*, 2002.

[30] Z.Sosin. *Nucl.Instr.Meth.A693, 170*, 2012.

[31] P.Kulig. *EPJ Web of Conferences 66, 03049*, 2014.

[32] LISE++ group at NSCL/MSU. *http://lise.nscl.msu.edu*, 2013.

[33] R.J.Charity. *Phys.Rev.C58, 1073*, 1998.

[34] K.Summerer et al. *Phys.Rev.C42, 2546*, 1990.

[35] T.Cap et al. *Phys.Scr.T154, 014007*, 2013.

[36] T.Cap et al. *Phys.Scr.89, 054005*, 2014.

[37] J.Lukasik and Z.Majka. *Acta Phys.Pol.B24, 1959*, 1993.

[38] S.Leray. *J.Phys.Colloques.47, C4*, 1986.

[39] G.Tabacaru et al. *Nucl.Phys.A764, 371*, 2006.

[40] W.Gawlikowicz. *Acta Phys.Pol.B28, 1687*, 1997.

[41] W.Gawlikowicz. *Report ZFGM-03-02, Jagiellonian University*, 2003.

[42] A.Sochocka. *PhD Thesis, Jagiellonian University*, 2009.

[43] J.Cugnon and D.L'Hote. *Nucl.Phys.A397, 519*, 1983.